

1 **Machine Learning for Metallurgy II. A Neural Network Potential**
2 **for Magnesium**

3 Markus Stricker,* Binglun Yin, Eleanor Mak, and W. A. Curtin

4 *Laboratory for Multiscale Mechanics Modeling,*

5 *École Polytechnique Fédérale de Lausanne, Lausanne, Switzerland*

6 (Dated: September 3, 2020)

Abstract

Interatomic potentials are essential for studying fundamental mechanisms of deformation and failure in metals and alloys because the relevant defects (dislocations, cracks, etc.) are far above the scales accessible to first-principles studies. Existing potentials for non-fcc metals and nearly all alloys are, however, not sufficiently quantitative for many crucial phenomena. Here, machine learning in the Behler-Parrinello Neural Network framework is used to create a broadly-applicable potential for pure hcp Magnesium (Mg). Lightweight Mg and its alloys are technologically important while presenting a diverse range of slip systems and crystal surfaces relevant to both plasticity and fracture that present a significant challenge for any potential. The machine learning potential is trained on first-principles DFT-computable metallurgically-relevant properties and is then shown to well-predict metallurgically-crucial dislocation and crack structures and competing phenomena. Extensive comparisons to an existing very good modified embedded atom method (MEAM) potential are made. These results demonstrate that a single machine learning potential can represent the wide scope of phenomena required for metallurgical studies. The DFT database is openly available for use in any other machine learning method. The method is naturally extendable to alloys, which are necessary for engineering applications but where ductility and fracture are controlled by complex atomic-scale mechanisms that are not well-predicted by existing potentials.

7 I. INTRODUCTION

8 Metal alloys are widely useful for many structural applications due to the presence and
9 behavior of the underlying fundamental defects in the crystalline lattice. That is, the atom-
10 istic structures of dislocations, interfaces, crack tips, grain boundaries, precipitates, and
11 vacancies, and their evolution and interactions determine the plastic flow behavior, creep,
12 fatigue, fracture toughness, radiation resistance, etc. that ultimately control the macroscopic
13 material performance. Understanding those structures, and their dependence on chemistry,
14 is crucial for optimizing the use of existing alloys and for designing new higher-performance
15 alloys. This necessitates atomic-scale simulations at the scales of the defects, which are
16 often far too large for the use of first-principles methods such as density-functional theory

* markus.stricker@epfl.ch

17 (DFT). The development of semi-empirical interatomic potentials that accurately capture
18 the structures, energies, and motion of the various defects is thus essential.

19 The development of interatomic potentials has a long history, with successes and limi-
20 tations, that is briefly reviewed in a companion paper [1]. Existing potentials for metals
21 become increasingly inaccurate with increasing complexity in both crystal structure and
22 chemistry. Relevant to the present paper is the case of elemental hexagonally close packed
23 (hcp) metals, where many potentials struggle to capture the full range of operative slip
24 systems (basal, prismatic, pyramidal I and II) and with limited quantitatively-accurate ex-
25 tensions to alloys [2–6]. The general issues with traditional potentials are leading to the
26 application of machine learning methods to fit the potential energy surface (PES) of a metal
27 without imposing a highly-restricted functional form [7–12]. The construction of a machine
28 learned potential consists of (i) choosing a suitable class of geometric representations (the
29 descriptors) to describe local atomic environments [13–17], (ii) developing a database of en-
30 ergies and forces of atomic structures using first-principles methods (the training dataset),
31 and (iii) applying a regression algorithm (e.g. neural network, kernel ridge regression) to
32 optimize the parameters in the machine learning framework to best-match the training
33 data. Since the number of descriptors and/or parameters is unlimited, the machine-learning
34 approaches provide a “parameter-rich” space that can capture the training dataset well.
35 However, since it is pure regression, machine learning potentials are not suitable for ex-
36 trapolation to structures that differ notably from those in the training dataset. It must be
37 recognized, however, that traditional interatomic potentials having fixed functional forms
38 with limited parameters (i) are also intrinsically limited in their ability to accurately fit
39 many properties, (ii) depend on the target properties and regression algorithms, and (iii)
40 involve user-imposed decisions regarding which properties are most important because all
41 desired properties cannot be achieved with sufficient accuracy.

42 For machine learning, a careful balance must be struck in selecting an appropriate lim-
43 ited set of descriptors, a limited set of fitting parameters, and a sufficiently large and diverse
44 training set, so as to achieve broad accurate performance without the overfitting that ex-
45 acerbates extrapolation errors. To circumvent the tedious task of curating an exhaustive
46 training data set while maintaining transferability, several semi-automated protocols have
47 been developed to sample the phase space of a material. *Active learning* methods have used
48 random perturbations of bulk crystalline structures to sample the phase space of Al, Mg

49 and an Al-Mg alloy space [18]. *Self-guided learning* has explored the phase space by using
50 randomized unit cells paired with a selection of the most diverse structures, and applied
51 to C, Si and Ti [19]. *On-the-fly learning* methods have combined DFT calculations with
52 machine learning for the calculation of melting points for Al, Si, Ge, Sn and MgO [20]. A
53 new hybrid approach combines an analytical bond order potential (BOP) form with a neural
54 network that adjusts the BOP parametrization depending on the specific environment [21].
55 This approach can improve extrapolations because the analytical form is smooth.

56 A key, and limiting, aspect of nearly all of the machine learning (ML) potentials gener-
57 ated to date is that the training data, and fitness of the potential, are mainly demonstrated
58 on basic properties of the bulk crystalline material [22]. Very few, if any, defects are con-
59 sidered. Structures in the training set and the predicted properties are associated with the
60 equilibrium geometry, elastic response of the bulk, vibrational properties, vacancies, sur-
61 faces, etc. and, in some cases, liquid-state information. These features are necessary but
62 far from sufficient for performing metallurgically-useful studies of the behavior of defects
63 in metals. For instance, the stable stacking fault energy (SSFE) for both fcc Ni and Cu
64 is very poorly predicted by all the machine learning methods analyzed in Ref. [22] because
65 the nature of the training set did not include configurations near this structure. The afore-
66 mentioned self-guided semi-automatic approaches using random perturbations are useful to
67 sample very-near bulk configurations but will not produce e.g. a stacking fault or a vacancy.
68 Yet, the SSFE is essential for modeling dislocations, and so none of the machine learning
69 potentials in Ref. [22] would be suitable for quantitative plasticity modeling, although that
70 was not the purpose of Ref. [22]. There are a few efforts extending beyond basic properties.
71 Kobayashi et al. [9] developed a neural network potential (NNP) for the Al-Mg-Si system
72 including many intermetallics, solute-solute interactions, and interfaces, and showed good
73 predictions for edge and screw dislocation structures, solute/dislocation interactions, and
74 in-situ precipitates; further development was shown by Imbalzano et al. [23]. The Gaussian
75 Approximation Potential (GAP) potentials for Fe [24] and W [25] included baseline data
76 needed for describing dislocations, and the GAP Fe potential was used to study the double-
77 kink nucleation process that controls plastic flow in bcc metals [26]. The hybrid Physically
78 Informed Neural Network (PINN) approach [21] showed application to an face centered cu-
79 bic (fcc) edge dislocation in Al. A NNP developed for Ti presented transformation pathways
80 from body centered cubic (bcc) to fcc crystal structure [12]. These recent works highlight

81 the promise of machine learning methods, but still remain fairly limited in metallurgical
82 scope.

83 In this paper we study Magnesium (Mg) as both an excellent complex testbed for machine
84 learning and because Mg is a very desirable structural material [27–29] due to a combination
85 of low density, high specific strength and availability [30]. Complexity arises because the
86 crystal structure is hcp so that the many different slip systems must be activated to enable
87 general plasticity according to the von Mises criterion [31], and various possible crack ge-
88 ometries may be susceptible to cleavage [32]. These issues are intimately tied to the low
89 ductility and low toughness of pure Mg, which severely limits its practical application. Re-
90 cent work shows that alloying Mg with dilute ($< 1\%$) additions of Rare Earth elements (Y,
91 Nd, Ce, Gd), Ca, and Mn, improves ductility at room temperature substantially. This has
92 been attributed to solute-accelerated cross-slip and double cross-slip of pyramidal $\langle \mathbf{c} + \mathbf{a} \rangle$
93 dislocations [33–35], demonstrating the intimate connection between detailed atomic-scale
94 dislocation processes in the alloy and the macroscopic behavior. But direct simulations
95 require scales far above those accessible by DFT. Simulation of this mechanism and other
96 mechanisms associated with flow and fracture remain necessary but thus require potentials
97 suitable for the simulations of hundreds of thousands of atoms. Furthermore, the potentials
98 must have an accuracy sufficient to capture very subtle energy differences between different
99 dislocations that ultimately govern the mechanical behavior of Mg. Early embedded atom
100 method (EAM) potentials for Mg failed dramatically in their descriptions of the pyramidal
101 dislocations [36] but MEAM potentials for pure Mg exist [4, 5] and the most recent ver-
102 sions [5, 6] are overall quite good. However, even the most recent MEAM for the important
103 Mg-Y [37] is not sufficiently accurate for all necessary quantities, making it unsuitable for
104 studying critical mechanisms in Mg alloys.

105 As the first essential step in overcoming the current limitations to atomistic studies of Mg
106 and its alloys, here we present a family of Behler-Parrinello Neural Network (BPNN) [13]
107 (or short NNP hereafter) machine learning potentials for pure Mg using the implementation
108 of the library `n2p2` [38]. The potentials are fitted with extensive first-principles DFT calcu-
109 lations of metallurgically-relevant properties. However, we intentionally restrict the training
110 database to (nearly) the same set previously used to fit MEAM potentials and then make
111 side-by-side comparisons of MEAMs and NNP. We control every step of the fitting process
112 with state of the art methods from the choice of the representation (symmetry functions),

113 the choice of the neural network topology, and the curation of the training data. Results
114 demonstrate that the family of NNP, and detailed analysis of one selected NNP denoted
115 as NNP63, is broadly superior to the best MEAM potentials when evaluated across a wide
116 range of metallurgical properties. The crucial pyramidal II $\langle \mathbf{c} + \mathbf{a} \rangle$ dislocation structure
117 remains imperfect, and restrictions on the use of the current potential are discussed. How-
118 ever, the NNP in general can be continually improved with an expanded training database,
119 augmented to avoid some of the extreme extrapolation problems, and, most importantly,
120 easily extended to Mg alloys.

121 The remainder of this paper is organized as follows. In section II the BPNN potential
122 framework is summarized and the fitting procedure is described. Additional details about
123 the DFT implementation used to build the training data base, and the range of structures
124 considered is presented. Section III compares the predictions of both NNP63 and MEAM
125 potentials against the DFT for a range of properties directly derivable from DFT, and rel-
126 evant for mechanical properties. In more detail, Section III A presents the results from the
127 fitting the neural network; Section III B presents material properties of which most under-
128 lying structures were part of the training set; Sections III C and III D each present results
129 on training set data (stacking fault energy curves and decohesion, resp.) and the related
130 applications to dislocation and fracture which demonstrate transferability of the potential.
131 Predictions using NNP63 are then made for dislocation geometries, basal dislocation Peierls
132 stress, and fracture (crack tip phenomena) for a range of orientations, with comparisons
133 to available DFT, experiments, and/or theoretical predictions. Section IV provides further
134 discussion of our results and summarizes the work including future possibilities for Mg-alloy
135 potentials.

136 II. METHODS

137 A. Neural network architecture and implementation

138 In this section we briefly outline the structure of a NNP in the formulation of Behler-
139 Parrinello [13]. All details and implementation of the neural network method employed here
140 are well-presented in the recent literature and the reader is referred to e.g. [13, 38–41].

141 Machine-learning potentials developed to date first assume that the total potential energy

142 of a system of N atoms can be represented as a sum of the energies of each atom $n = 1, \dots, N$,
 143 with the energy of each atom depending on the local environment around the atom,

$$E_{\text{tot}} = \sum_{n=1}^N E_n. \quad (1)$$

144 This assumption is also underlying any other empirical potential and enables efficient ap-
 145 plication of the methods to large system sizes, as opposed to specific potentials for problems
 146 with a fixed size [42]. The neural network potential formulation of Behler and Parrinello [13]
 147 consists of the choice of the atomistic structural representation called the symmetry func-
 148 tions, the number of hidden layers in the neural network, and the number of hidden nodes per
 149 layer in the network. For a dense two layer neural network as used here with the symmetry
 150 functions denoted as G_i , the local atomic energy E_n is described as

$$E_n = f_1^3 \left(b_\ell^3 + \sum_{\ell=1}^{M_{\text{layer},2}} w_{k\ell}^{23} \cdot f_k^2 \left(b_k^2 + \sum_{k=1}^{M_{\text{layer},1}} w_{jk}^{12} \cdot f_j^1 \left(b_j^1 + \sum_{i=1}^{M_{\text{sym}}} w_{ij}^{01} \cdot G_i \right) \right) \right), \quad (2)$$

151 where $f(\cdot)$ are the so-called activation functions, $M_{\text{layer},i}$ denotes the number of nodes in
 152 the i -th hidden layer, M_{sym} is the number of symmetry functions used to represent local
 153 atomic environments. The quantities $\{w_{ni}\}$ and $\{b_i\}$ are the so-called weights and biases,
 154 which are determined by fitting the total energy modeled according to Eq. 1 to a training
 155 dataset of structures, total energies, and individual atomic force components. The i - th
 156 component $F_{n,i}$ of the force on atom n is computed as $F_{n,i} = -\partial E_{\text{tot}} / \partial x_{n,i}$.

157 The structural representations of the atomic environment are dictated by the symmetry
 158 functions. The BPNN framework defines radial and angular symmetry functions of the forms

$$G_i^{\text{rad}} = \sum_{i \neq j} e^{-\eta(r_{ij} - r_s)^2} f_c(r_{ij}) \quad (3)$$

$$G_i^{\text{ang}} = 2^{1-\zeta} \sum_{j,k \neq i} (1 + \lambda \cos \theta_{ijk})^\zeta e^{-\eta(r_{ij}^2 + r_{ik}^2 + r_{jk}^2)} f_c(r_{ij}) f_c(r_{ik}) f_c(r_{jk}), \quad (4)$$

159 where $r_{ij} = |\mathbf{r}_j - \mathbf{r}_i|$ is the distance between two atoms i and j , θ_{ijk} the angle between
 160 three atoms i, j, k , f_c is a smooth cutoff function and η , r_s , λ and ζ are pre-defined hyperpa-
 161 rameters. Here, we employ 27 radial and 5 angular symmetry functions; this is a heuristic

162 design choice based on goals of avoiding overfitting and having acceptable computational
163 costs (cf. Appendix A for the specific hyperparameters). The selection of the specific func-
164 tions is made as follows. An initially very large number M of possible symmetry functions is
165 considered. The training dataset of atomic structures is then specified. Each atom in each
166 structure has a local atomic environment; across the entire training set there are a total
167 of N atoms and thus N local environments (some of which may be identical). By evalu-
168 ating the M candidate symmetry functions centered on each atom in the training dataset
169 a so-called *feature matrix* is created that consists of the M symmetry functions (columns)
170 by N atomic environments (rows). An unsupervised selection algorithm based on a CUR
171 matrix decomposition [23] then determines the 32 most *valuable* symmetry functions ($\ll M$
172 columns) of the feature matrix, i.e. those with the highest information content with respect
173 to all the N environments in the training structures. This selection constitutes the input
174 layer of the NNP. The CUR method could also be used to provide an error measure for the
175 selection, from which the number of symmetry functions would then be an outcome. Note
176 that the selection of symmetry functions is intimately tied to the training dataset; if the
177 training dataset is increased or filtered then the optimal set of symmetry functions might be
178 different. In practice, the use of a large number of bulk-like atomic environments in metals
179 leads to fairly small differences in the selected set of symmetry functions when the training
180 dataset is extended by including additional structures.

181 The employed neural network consists of an input layer with 32 symmetry functions,
182 two hidden layers with 20 nodes each, and the final layer with one neuron representing the
183 energetic contribution an atomic environment (Eq. 2). The hyperbolic tangent is used as an
184 activation function. This chosen topology results in 1101 fitting parameters, which is the
185 combined number of weights and biases of the network.

186 After selecting the symmetry functions and fixing the topology of the neural network,
187 the determination of the weights $\{w_{ni}\}$ and biases $\{b_i\}$ is done with supervised learning to
188 minimize an error function Γ equal to the sum of the squares of the differences between the
189 NNP and DFT energies and forces. Specifically, for N_{struct} structures in the training set [39],
190 the error measure is

$$\Gamma = \frac{1}{N_{\text{struct}}} \sum_{i=1}^{N_{\text{struct}}} \left((E_{\text{NNP}}^i - E_{\text{DFT}}^i)^2 + \frac{\beta}{3N_{\text{atom}}^i} \sum_{j=1}^{3N_{\text{atom}}^i} (F_{j,\text{NNP}}^i - F_{j,\text{DFT}}^i)^2 \right) \quad (5)$$

191 where E and F represent the energy of, and forces on individual atoms in, a structure,
 192 respectively. β (in \AA^2) is a fixed parameter during training that allows for relative weighting
 193 of forces versus energies; here we use $\beta = 10 \text{\AA}^2$. The quality of the optimization is then
 194 measured by separately evaluating of the root-mean-square errors of the energy and forces,

$$\text{RMSE}(E) = \sqrt{\frac{1}{N_{\text{struct}}} \sum_{i=1}^{N_{\text{struct}}} (E_{\text{NNP}}^i - E_{\text{DFT}}^i)^2} \quad (6)$$

$$\text{RMSE}(F) = \sqrt{\frac{1}{N_{\text{struct}}} \sum_{i=1}^{N_{\text{struct}}} \sum_{j=1}^{3N_{\text{atom}}^i} \frac{1}{3N_{\text{atom}}^i} (F_{j,\text{NNP}}^i - F_{j,\text{DFT}}^i)^2} \quad (7)$$

195 The fitting (or *training*) of NNPs is done with a Kalman filter [43] as implemented in
 196 n2p2 [38] for 400 epochs (iterations). The number of epochs is based on initial tests. For the
 197 chosen symmetry functions, neural network topology, and the dataset the gradient of the
 198 error function (Equation 5) with respect to epochs becomes sufficiently small at 400 epochs
 199 while overfitting is avoided. Changes in the initial values of $\{w_{ni}\}$ and $\{b_i\}$ and/or of the
 200 subset of structures used in the fitting lead to different final NNPs with different results
 201 for material properties. Comparisons among these NNPs enables assessment of the broader
 202 capability of the NNPs and for determining when the NNPs are being used in regions of
 203 inaccurate extrapolation. If the different NNPs deviate by some meV/atom on any given
 204 structure, then the differences are well below the typical errors between the NNPs and the
 205 DFT (a few meV/atom). The different NNPs are also used to compute material properties
 206 that involve energy differences between a defect/deformed and a reference state. If the
 207 errors in the absolute energies of both reference and defect states differ in sign, then the
 208 material property can deviate more than anticipated from the general root mean squared
 209 error (RMSE) of the NNP. Assessing these latter issues are essentially validation steps
 210 outside of the generic machine learning formulation itself.

211 The choice of the training dataset with the function for optimization (Eq. 5) defines the
 212 mathematical optimization problem. This might seem trivial but is important. Choosing
 213 many similar structures implicitly steers the optimization towards favoring a low error on

214 those structures. Also, the loss function here (Eq. 5) contains an implicit weighting of
215 structures with high energies (typically structures with large numbers of atoms). Any step
216 in the optimization that reduces the error of a large structure also reduces the total error by
217 a factor scaling with the number of atoms. Most of the energy of a solid-state structure is
218 dominated by the cohesive energy (cf. Figure 1, (a) and (b)) and reducing that error for large
219 structures reduces the overall RMSE. However, defect formation energies are calculated as
220 the difference between the defect structure and the reference structure. The defect structure
221 may involve many (10s or 100s) of atoms that are away from the defect and near the bulk
222 reference configuration. This issue points to the value of adding atomic forces through non-
223 equilibrium structures into the overall optimization as a means capturing local behavior.
224 Many of these points can not be addressed here, and exist because the standard methods
225 such as the BPNN as implemented in `n2p2` [38] were mainly developed for applications to
226 molecules rather than solids such as bulk metals. Contrary to a database of bulk metals,
227 a database of molecules is often very homogeneous with respect to the number of atoms
228 per structure. As the application of ML methods to solids expands, future optimization
229 methods and codes may address these issues.

230 B. Training dataset and DFT details

231 A suitable training dataset should span the atomic environments encountered in a wide
232 range of crystalline defects so that the potential is best-suited to interpolate between those
233 environments. Here, we use a training dataset for the NNP that is nearly the same as used
234 for prior MEAM-type potentials. Typical input data for fitting a MEAM potential comprises
235 values for lattice constants, elastic constants, stacking faults, generalized stacking fault en-
236 ergy curves, decohesion curves and surface energies for various crystallographic planes, often
237 with a combination of first-principles calculations and experimental values [5]. Here, for the
238 NNP, we use the same underlying data but fit only energies and forces, from which material
239 properties are then derived. Thus, instead of using a *big data* approach, we incorporate
240 metallurgical knowledge by choosing relevant structures for mechanical properties. A big
241 data approach might include many types of random structures which would not be used in
242 a traditional approach, e.g. liquid structures which are snapshots from a trajectory at a
243 specific temperature. But, as noted earlier, the inclusion of large structures may drive the

244 NNP toward capturing those structures, and those structures may not be sufficient for accu-
245 rate representation of crystalline defects. The addition of further structures to the training
246 dataset is always possible.

247 The training dataset developed here consists of atomic structures whose energies are used
248 for calculating the energy-volume curve, elastic constants (C_{ij}), cohesive energy, generalized
249 stacking fault energy (GSFE) curves (basal, pyramidal I and pyramidal II), stable stacking
250 fault energies (basal, pyramidal I and pyramidal II) that can involve relaxations missing in
251 the standard GSFE, decohesion curves (basal, pyramidal I and II), and fully-relaxed surface
252 energies. In addition, beyond the above data typically used for the MEAM potential, we find
253 it necessary to include rod and cuboidal structures containing corners and edges of several
254 high symmetry planes to obtain physical behavior at atomically-sharp crack tips. The com-
255 plete DFT dataset consists of 443 structures with a total of $N=12268$ atom environments.
256 As discussed earlier, the number of atomic environments in the dataset defines the N rows
257 of the feature matrix. Similar/identical atomic environments, e.g. from a bulk material, do
258 not need a different set of optimal symmetry functions; they can be described with the same
259 symmetry functions without loss of information. But given the current function (Eq. 5), the
260 number of individual atoms (and therefore the environments) does change the optimization
261 by implicit weighting. The entire dataset is accessible on `MaterialsCloud` [44].

262 All first-principles calculations are performed using DFT as implemented in the Vienna
263 Ab Initio Simulation Package (VASP) [45, 46] within the generalized gradient approximation
264 (GGA) and using the Perdew-Burke-Enzerhof (PBE) exchange correlation functional [47].
265 Core electrons are replaced by the projector augmented wave (PAW) pseudopotentials [48]
266 with Mg ($3s$) as the valence state. The valence-electron eigenstates are expanded using
267 a spin-polarized plane-wave basis set with a cutoff energy 400 eV. In reciprocal space, a
268 Γ -centered Monkhorst-Pack [49] k -mesh is used with line density consistent across all ge-
269 ometries. The interval between the neighboring k -points along each reciprocal lattice vector
270 \mathbf{b}_j is $0.02\pi \text{ \AA}^{-1}$ (in VASP, $\mathbf{a}_i \cdot \mathbf{b}_j = \delta_{ij}$) and the k -mesh for the Mg 2-atoms primitive
271 hcp cell is $36 \times 36 \times 19$. A second-order Methfessel-Paxton method [50] with a smear-
272 ing parameter of 0.2 eV is used. The employed DFT parameters yield lattice constants
273 ($a = 3.198 \text{ \AA}$, $c/a = 1.627$) and elastic constants (see Table I) in very good agreement with
274 experiments [51].

275 It is important to use well-converged and consistent DFT calculations. Any computa-

276 tional inconsistencies across the DFT are translated directly into the resulting NNP, i.e.
277 the machine learning potential is trying to learn inconsistencies yet treating them as real.
278 As usual, approximations in the DFT carry over into the NNP; the NNP can only be as
279 accurate as the DFT training set.

280 **III. RESULTS**

281 In the following we mainly compare one fitted NNP63 to the DFT dataset and to various
282 material properties directly derivable from DFT energies. However, results for all 129 NNP
283 are also shown in a number of cases. The single choice of NNP63 for the majority of studies
284 presented here is based on several assessments. First, the RMSEs of energies and forces
285 (Eqs. 6 and 7) are on the order of meV/atom and meV/Å respectively. Second, the material
286 properties (cf. Table I) match reasonably against DFT values. Additional tests, not shown
287 here, with rod and cuboid shapes were also performed and no unexpected or anomalous
288 behavior was found. In comparisons below, we start with basic material properties and then
289 extend to properties outside of the training set. We then examine stacking fault energies
290 and predicted dislocation structures, followed by decohesion energies and predicted crack-tip
291 behavior relevant to fracture.

292 All the following simulations are performed using LAMMPS [52] with n2p2 [38] and
293 Ovito [53] is used for the visualization of atomic structures.

294 **A. NNP63 versus DFT training set**

295 Figure 1 presents the energies, energies per atom, and forces for all of the structures in
296 the DFT dataset as computed using our final single choice for the Mg NNP63 versus the
297 DFT training and testing inputs. The fit is good, especially given the range of energies
298 (Figure 1 (a)) for the different structures: RMSEs are 6.68 meV/atom and 12.8 meV/Å for
299 energy and forces, respectively. Large deviations from the ideal energy in the center of
300 Figure 1 (b) belong to structures with two atoms only and are very high in total energy, i.e.
301 a large difference does not matter here, since the energies are on the order of 1 eV above
302 bulk equilibrium (cf. discussion along Figure 4). Similar results are obtained for all other
303 NNP generated. These errors are in expected range with machine learned potentials for the

304 prediction of atomic energies and forces for metals based on diverse training sets [9, 24–26].
 305 The total energies of each structure are shown, rather than energy per atom, because it is
 306 the total energies that enter the loss function (Eq. 5). Forces are presented as per atom
 307 per direction, again because that is how they enter the loss function (Eq. 5). As mentioned
 308 in section II, structures with large energies bias the optimization towards minimizing the
 309 absolute errors of these structure, not the relative errors. Our training set includes structures
 310 containing from 2 to 216 atoms, with 2 atom structures related to bulk properties and
 311 the 216 atom structures related to structures with corners, i.e. rod shapes (surfaces in
 312 two directions, periodic in one direction) and cuboids (surfaces in all three directions).
 313 The implicit weighting of structures with a higher number of atoms is, however, partially
 314 compensated by the larger number of bulk-related structures as compared to surfaces and
 315 corners in the present dataset.

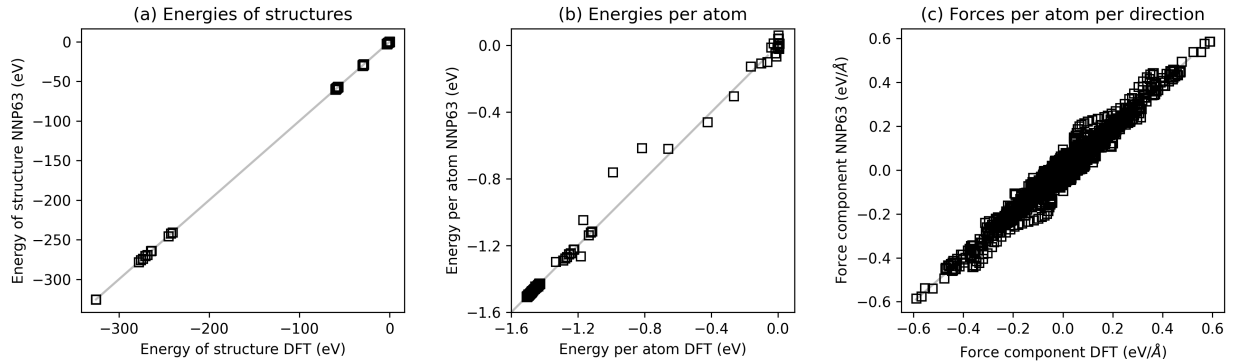


FIG. 1. NNP63 vs. DFT calculated energies of structures (a), energies per atom (b), and forces (c) after training.

316 B. Basic material properties

317 The accuracy of an interatomic potential is assessed mainly by its ability to reproduce ma-
 318 terial properties that are either known from experiments or are computed/derived from DFT
 319 energies. For machine-learning potentials, only DFT is the reference; deviations of DFT-
 320 derived properties must be resolved independently of any DFT-derived machine learned
 321 potential. For elemental metals, the main material properties considered by most tradi-
 322 tional potentials are the lattice constants, elastic constants, cohesive energy, vicinal surface

323 energies, and vacancy formation energy. Occasionally, the stable and unstable stacking fault
324 energies for important slip modes are also evaluated or fitted.

325 Furthermore, the standard error assessment of a NNP after training (e.g. Figure 1) is
326 not necessarily meaningful. Standard material properties are defined in terms of energy
327 differences between states. So, errors in absolute energy having a different sign may lead
328 to a poor property prediction. Or, when the errors in absolute energy are not small com-
329 pared to the energy difference, then a poor property prediction is obtained. The latter is
330 especially relevant for elastic constants, which require energy differences between structures
331 that differ only by very small strains - the use of larger strains introduces nonlinearities that
332 violate linear elasticity. Hence, potentials must be carefully validated on various material
333 properties. Standard potentials are often directly fit to the material properties rather than
334 fitting energies from which properties are then derived, as done for the NNP.

335 Table I presents a range of basic material properties of Mg from experiments, as computed
336 from DFT, our selected NNP63 potential, and two existing MEAM potentials developed
337 previously by our group [5, 6]. Overall, the properties of NNP63 agree well with the DFT
338 reference values, which in turn agree well with experiments. One notable deviation is a
339 slightly smaller c/a ratio; deviations in c/a from the ideal value determine the Burgers
340 vector associated with twinning dislocations and so this deviation in c/a is not as negligible
341 as it might otherwise appear. Another notable deviation is the larger value of C_{11} . Since
342 elastic constants determine elastic energies, this deviation can affect dislocation structures
343 and other defect properties. On the other hand, the stable stacking fault energies for the
344 pyramidal I and pyramidal II planes are much closer to DFT than either of the MEAM
345 potentials, and these quantities are crucial for establishing the relative stability of pyr.I
346 and II dislocations that are believed to hold the key to ductility in Mg and its alloys. The
347 agreement for properties in the upper half of the table is expected because the associated
348 structures are contained in the training dataset.

349 Table I also shows some additional properties that are not derived directly from structures
350 and energies in the training set. Examination of such structures provides some indication
351 of transferability of a potential to unknown atomic environments. Here, the tension twin
352 interface, which is a very low-energy planar structure, is well-predicted by NNP63 while
353 the MEAM potentials shows a larger error. Similarly, the vacancy formation and migration
354 energies – involving coordinations that are not directly contained in the training set struc-

355 tures – are also well-predicted by NNP63. In contrast, the MEAM values are much worse,
356 with the migration barriers being very poor and not sufficient for any realistic studies of
357 diffusion-related phenomena.

358 Finally, while our primary interest is in solid-state Mg and the crystalline defects that
359 control mechanical properties, we have also examined the melting point of NNP63 to further
360 demonstrate the scope of possible applications. We estimate the melting point by performing
361 a periodic dual-phase crystal-liquid system with 8064 atoms and a nominally flat crystal-
362 liquid interface with the normal coinciding with the c -axis, i.e. $\mathbf{n} = [0001]$. A constant
363 average interface position over time is achieved at a estimated melting point of $T_m \approx 900$ K.
364 No liquid or random configurations of atoms were part of the training set and therefore these
365 simulations additionally demonstrate transferability of the potential even beyond the solid
366 state.

367 The above results are shown for the selected NNP63. Executing the optimization algo-
368 rithm using different training sets (90% of the total set of structures and energies) leads to
369 different final weights and biases, and hence different final NNPs. Limited studies indicate
370 that variations in the initial choices of the weights and biases, but using a fixed training set,
371 result in small variations in the final RMSE. The variations among NNPs thus arise from
372 the differences in the choice of the 90% of structures used for training. Using our overall
373 set of structures and energies, we have developed 129 different NNPs for Mg that should
374 be nominally identical. Figure 2 shows the mean and standard deviation of a range of
375 material properties, including those in Table I, computed from these 129 NNPs, along with
376 the properties obtained from the MEAM potentials; here we show the relative deviation
377 versus DFT-computed properties rather than the properties themselves. The average of
378 NNPs predictions are, overall, in better agreement with DFT than the MEAMs across most
379 material properties. The MEAMs does provide better properties in a few cases, generally
380 those that were directly fit. The standard deviation in properties across all 129 NNPs is
381 typically $\pm 10\%$ or less, and the NNPs deviate from DFT by no more than $\pm 12\%$ across all
382 material properties. We note clearly that this standard deviation is not a true statistical
383 measure – the different NNPs are all trained on very similar training sets and so results
384 are not representative of statistically-independent random variables or samplings. A more
385 relevant standard deviation quantity can be estimated using the methodology in [62]. Here,
386 the standard deviation is merely used to indicate the range of property values starting from

TABLE I. Pure Mg material properties from experiments, *ab initio* calculations (evaluated on the same dataset used for training the neural network potential), NNP63, the empirical MEAM potential (here denoted MEAM1 [54]), and another MEAM fit (here denoted as MEAM2 [6]). Stacking fault values are for relaxed ($\sigma_{3j} = 0$) as described in [55]. All values other than DFT have been calculated with the same protocol. The additional values in the lower part of the table are not part of the training set.

Mg properties	Exp.	DFT	NNP63	MEAM1 [5]	MEAM2 [6]
a (Å)	3.209 (300K) [56]	3.190	3.186	3.187	3.186
c/a	1.624 (300K) [56]	1.627	1.613	1.623	1.622
E_c (eV/atom)	-1.51 [57]	-1.51	-1.51	-1.51	-1.51
C_{11} (GPa)	63.5 [58]	61	72	66	66
C_{12} (GPa)	25.9 [58]	28	31	24	25
C_{13} (GPa)	21.7 [58]	22	27	20	22
C_{33} (GPa)	66.5 [58]	64	68	71	70
C_{44} (GPa)	18.4 [58]	18	19	18	18
Stacking fault energies (mJ/m ²)					
γ_{sf} Basal II	33 [59]	34	31	23	20
γ_{sf} Pyr. I SF2	-	161	157	169	154
γ_{sf} Pyr. II SF	-	165	155	200	169
Surface energy (mJ/m ²)					
Basal (0001)	-	549	583	568	562
Prism (10 $\bar{1}$ 0)	-	624	644	583	569
Pyramidal I (10 $\bar{1}$ 1)	-	640	663	616	622
Pyramidal II (11 $\bar{2}$ 1)	-	732	746	652	639
Additional values					
Tension twin					
Interface E (mJ/m ²)	-	128.1 [60]	118.8	148.0	132.3
Vacancy energies (eV)					
formation	0.79 ± 0.03 [61]	0.796	0.735	0.908	0.667
migration barrier basal	-	0.397	0.436	0.616	0.601
migration barrier pyr	-	0.416	0.470	0.641	0.616
Melting point T_m (K)	923	-	~ 900	-	-

387 different specific training sets. Overall, most of the 129 NNPs perform better than the
 388 MEAMs, and the MEAMs can show substantial deviations from DFT, particularly for some
 389 surface and stacking fault energies.

390

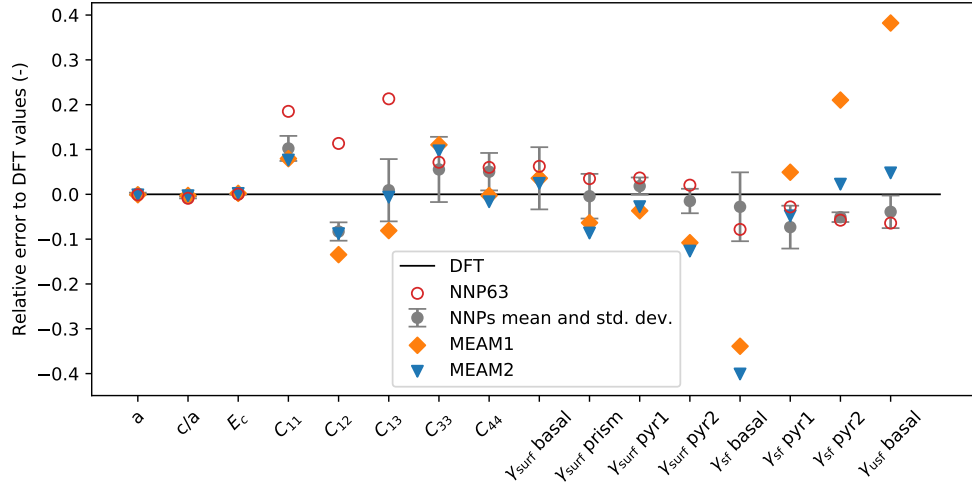


FIG. 2. Relative errors for various material properties with respect to DFT of NNP63 (red unfilled circles), the mean and standard deviation of the entire family of NNPs (gray), and two MEAMs (orange diamond shape and blue triangle).

391 The MEAM predictions for the stable stacking fault energy of the basal plane γ_{sf} show
 392 particularly large relative errors of $\approx 40\%$. Such an error has significant consequences for
 393 plasticity in Mg and its alloys because basal slip is the dominant slip system in Mg. The low
 394 MEAM stacking fault energy leads to a wider dissociation of the basal $\langle \mathbf{a} \rangle$ dislocation. This
 395 may affect the strengthening of basal slip upon alloying, which is important for reducing the
 396 plastic anisotropy (ratio of pyramidal strength to basal strength) that can be important for
 397 ductility. In addition, prismatic $\langle \mathbf{a} \rangle$ slip, having the same Burgers vector as the basal $\langle \mathbf{a} \rangle$ slip,
 398 can be important in the plasticity of textured Mg sheet materials. But it is understood to
 399 occur only via cross-slip of screw dislocations from the basal plane to the prism plane. This
 400 cross-slip requires thermally-activated recombination of the basal partial dislocations, and
 401 the energy barrier scales inversely with the stacking fault energy. We make these remarks
 402 to demonstrate that a deep understanding of metallurgical mechanisms is critical to the
 403 assessment of any interatomic potential, and that a broadly-applicable potential must be
 404 sufficiently accurate for many properties.

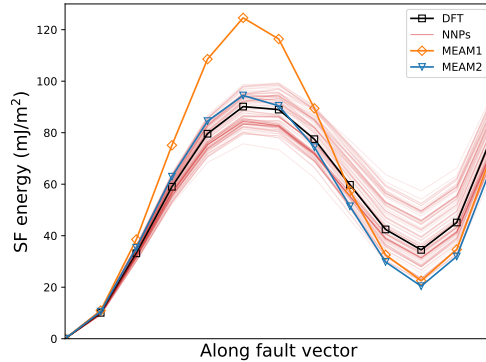


FIG. 3. Generalized stacking fault energy curves for the basal plane from DFT (black), multiple NNPs (red) and two MEAM potentials (orange and blue).

405 As another example showing the generally good agreement of the 129 NNPs versus refer-
 406 ence training data is presented in Figure 3. This figure shows the generalized stacking fault
 407 energy curve for basal slip as predicted by DFT, the two MEAMs potentials, and multiple
 408 NNPs. All the NNPs perform much better than the original MEAM1 potential over the en-
 409 tire range of slip, but especially for the unstable stacking fault energy γ_{usf} that is important
 410 for fracture (see Section IIID). Many of the NNPs provide a better basal stable stacking
 411 fault energy than either of the MEAMs, as noted above. Figure 3 further shows that it is
 412 not only the extremal values presented in 2 that are in good agreement, but rather the entire
 413 curves. The entire GSFE curve enters into the widely-used Peierls-Nabarro model for the
 414 dislocation structure (distribution of Burgers vector along the slip plane), and so is valuable
 415 to capture well.

416 As with traditional potentials, the choice of one particular NNP over any of the other
 417 NNPs is based on heuristics associated with preferred applications of the potential. It
 418 would be possible to determine a single *best* overall NNP by minimizing the relative error
 419 with respect to DFT across all basic material properties computed, but this also implies a
 420 relative weighting of the importance of structures according to their energies. So, there is
 421 no unbiased way to select a preferred NNP.

422 It is inherent in the formulation that NNPs can fail in extrapolation, with the typical
 423 example being failure under high compression. Figure 4 shows the equation of state, i.e.
 424 the energy per atom versus volume at fixed c/a ratio, as predicted by all the NNPs and
 425 with the reference/training DFT values also shown. Indeed, below the minimum relative

426 volume 0.9 in the DFT training set, the NNPs show wide variability, and with some cases
 427 showing unstable collapse of the structure below ~ 0.85 . Such behavior does not occur
 428 for the two MEAMs potentials because these potentials impose an ad-hoc strongly-repulsive
 429 pair-potential precisely to achieve reasonable behavior in compression. In fact, in the original
 430 EAM formalism, the pair-potential was purely repulsive [63, 64]. Three aspects about this
 431 behavior merit discussion. First, in many application cases outside of shock loading, this
 432 unphysical domain will never be encountered – in the region where NNPs remain accurate,
 433 the energies per atom and forces are too high for configurations to enter into the unstable
 434 domain. For instance, we have executed an extended molecular dynamics (MD) simulation at
 435 a temperature slightly below melting, and examined the global and local energy fluctuations
 436 as predicted by the selected NNP63 and by the MEAM1 potential. We find no statistical
 437 differences at all. So, no atom pairs are ever encountering the close separations at which
 438 NNP63 becomes unstable. Second, it is trivial to add a strongly repulsive pair potential
 439 to the NNPs formalism that operates only in this rarely-sample region of phase space. For
 440 instance, a Morse potential [65] of the form $V(r) = D_e [1 - \exp(-(r - r_0)/a_0)^2 - 1]$ with
 441 $r_0 = 0.9a$, a small a_0 , and large D_e will provide a strong repulsive contribution that will
 442 only be invoked if rare atom pairs attempt to move to within $0.9a$ (again, rare under nearly
 443 all situations). Third, the lowest value of the DFT results presented in Figure 4 is at 0.9
 444 relative stretch of the unit cell. The reason for this is that lower values of relative stretches
 445 do not converge in DFT. Hence adding DFT data points below 0.9 is not possible. One
 446 way to add datapoints below 0.9 would be by manually extrapolating the repulsive part, which
 447 is manual intervention based on the assumption of repulsion without knowing the actual
 448 values. A test training using such a strategy yielded the expected result: the repulsive
 449 part is well-predicted. Thus, this common failure of the NNPs in high compression is easily
 450 rectified but also of very limited importance in realistic applications.

451 The material properties for the chosen potential NNP63 in Figure 2 demonstrate that
 452 using the mean and standard deviation of a family of NNPs can be misleading. These
 453 quantities suggests that one can find a single potential for which all properties fall within
 454 the mean and standard deviation, which is not the case in general. Selecting a single NNP
 455 thus involves some external decision by the developer. For NNP63, the lattice parameters (a ,
 456 c/a) and cohesive energy (E_c) all show a very low relative error but the elastic constants and
 457 stacking fault energies have large errors well outside the standard deviation across the entire

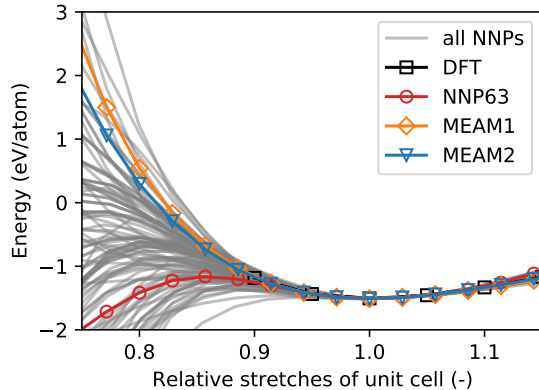


FIG. 4. Equation of state for all NNPs, the DFT reference (black squares), the selected NNP63 (red circles), and the two MEAMs (orange diamond, blue triangle).

458 family of NNPs. It should also be noted, however, that the relative errors of the MEAM
 459 potentials also show some significant errors across all the properties studied and require an
 460 external decision by the developer. An overview of the flexibility of classical interatomic
 461 potentials in fitting material parameters can be found in [66] where the authors optimize
 462 traditional fixed functional forms and assess the trade-offs between accurate modeling of
 463 different material properties.

464 C. Plasticity: stacking faults and dislocations

465 Plastic deformation in crystalline metals is mediated by dislocations. Many aspects of
 466 dislocation structures depend on the stable and unstable stacking fault energies, and on
 467 the overall generalized stacking fault energies for slip over entire crystallographic surfaces
 468 associated with dislocation slip planes. Thus, the first step in accurate modeling of actual
 469 dislocations is accurate modeling of the GSFs and stable stacking faults. We note that
 470 the GSFs are computed by relative in-plane sliding of blocks of material, with relaxation
 471 only of the stress normal to the fault plane. This procedure does not allow atomistic relax-
 472 ations on either side of the fault, but such relaxations are crucial for pyramidal slip in hcp
 473 materials [33]. Figure 5 shows the GSFs for the basal, prism, pyramidal I and pyrami-
 474 dal II planes. The NNP63 predictions are in generally very good agreement with the DFT
 475 whereas the MEAM1 potential is rather poor in all cases while the recent MEAM2 is nearly
 476 comparable to the NNP but still with some notable deviations. As noted earlier for basal

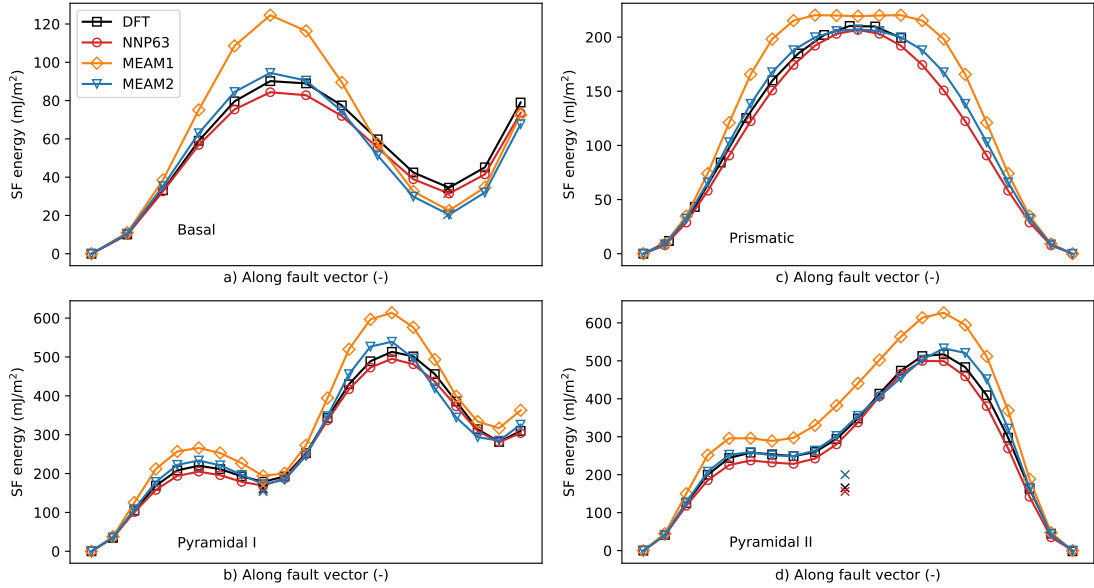


FIG. 5. Generalized stacking fault energy curves for basal, prism, pyramidal I and pyramidal II planes; comparison between DFT, NNP63 and the two MEAM potentials. The prismatic DFT values are not part of the training set. Fully relaxed stable stacking faults are indicated with an 'x' in the respective color.

477 slip, the errors in unstable stacking fault energies for the MEAM1 potential have notable
 478 consequences for fracture behavior, as discussed in the next subsection. The stable stacking
 479 fault energies are also shown in Figure 5 (indicated by small x's); especially the pyr. II case
 480 shows a difference of a factor 1.5 – 2 for the out-of-plane relaxations vs. rigid shift value.
 481 The differences versus DFT were discussed earlier.

482 The GSFE for prismatic slip was not in the training set and so is a true prediction.
 483 The absence of any local minimum at the symmetric midpoint has key consequences for the
 484 stability and structure of the prismatic dislocations. The spurious shallow local minimum
 485 predicted for the MEAM1 potential leads to the prediction of a stable $\langle \mathbf{a} \rangle$ Burgers vector
 486 screw dislocation on the prism plane, while DFT shows such a dislocation to be unstable
 487 relative to the $\langle \mathbf{a} \rangle$ screw dislocation on the basal plane. In contrast, the NNP63 potential is
 488 in agreement with DFT, predicting that the $\langle \mathbf{a} \rangle$ prism screw dislocation is not stable. The
 489 prismatic $\langle \mathbf{a} \rangle$ edge dislocation is stable for all potentials. We simulate the critical resolved
 490 shear stress, or Peierls stress, to initiate glide for the prismatic edge dislocation as $\sigma_P \approx 4$
 491 MPa, in line with expectations from the literature [67].

492 We now examine some of the stable dislocation core structures predicted by NNP63.
493 Dislocations control essentially all of the plastic flow phenomena in metals, and so are
494 responsible for the remarkable combination of strength and toughness of metal alloys. The
495 mechanical behavior at the macroscopic scale is then directly determined by the detailed
496 atomistic structure of the dislocations in the metal.

497 All dislocation geometries are constructed using the same protocol. For a specified Burg-
498 ers vector \mathbf{b} and line direction $\boldsymbol{\zeta}$, a cuboidal simulation cell is constructed with x along the
499 glide direction, y along the line direction $\boldsymbol{\zeta}$, and $z = \mathbf{b} \times \boldsymbol{\zeta}$ normal to the glide plane. The
500 length along y is the minimum periodic length for the given line direction and Burgers vector,
501 and periodic boundary conditions are applied in the line direction. The other two dimensions
502 are $L_x = L_z = 300$ nm. Two partial dislocations are introduced at a separation distance of
503 ~ 10 Å [55] and all atoms are displaced according to the anisotropic elastic Volterra fields of
504 the two partial dislocations, as implemented in [68]. The positions of all atoms within a dis-
505 tance $\sim 2r_c$ (where r_c is the cutoff of the potential) from the outer boundaries are held fixed
506 at the anisotropic elastic Volterra solution according to a perfect dislocation. The remain-
507 ing interior atoms are then relaxed to the minimum-energy configuration via the conjugate
508 gradient method. Only the pyr.I screw dislocation is obtained differently, as follows. A
509 relaxed dissociated pyr.II screw dislocation core (obtained as described above) is heated up
510 to 100 K and MD simulation is executed with the outer atoms held fixed (the elastic field of
511 the pyr.I and II screws being identical). Snapshots from the MD trajectory are saved peri-
512 odically. Each of those snapshots is then relaxed to $T = 0$ K minimum-energy configuration
513 and the structure is analyzed. This procedure allows for a meaningful comparison of energy
514 differences between pyr.I and II dislocation cores generated with exactly the same boundary
515 conditions. Since the pyr.II core has a lower energy, it is the most common outcome, but
516 pyr.I cores do occur.

517 For all dislocations, the resulting structures are analyzed using the Nye tensor [69] as
518 implemented in [68], which compares the dislocation structure to a reference structure and
519 reveals the flux of Burgers vector passing through any closed loop normal to the dislocation
520 line. The edge and screw components of the Nye tensor are computed at each atomic posi-
521 tion. We note that analyses based on the differential displacement [70], Common Neighbor
522 Analysis (CNA) [71] or the dislocation extraction algorithm [72] would also be possible and
523 yielded similar results in limited tests.

524 Figure 6 and Figure 7 show the dislocation core structures with superimposed Nye tensor
 525 components of the basal $\langle \mathbf{a} \rangle$ edge and screw dislocations, respectively, as predicted by DFT
 526 and NNP63. The Nye tensor components for DFT are recomputed from [73]. For ease of
 527 comparison, we have aligned the right partials in all figures.

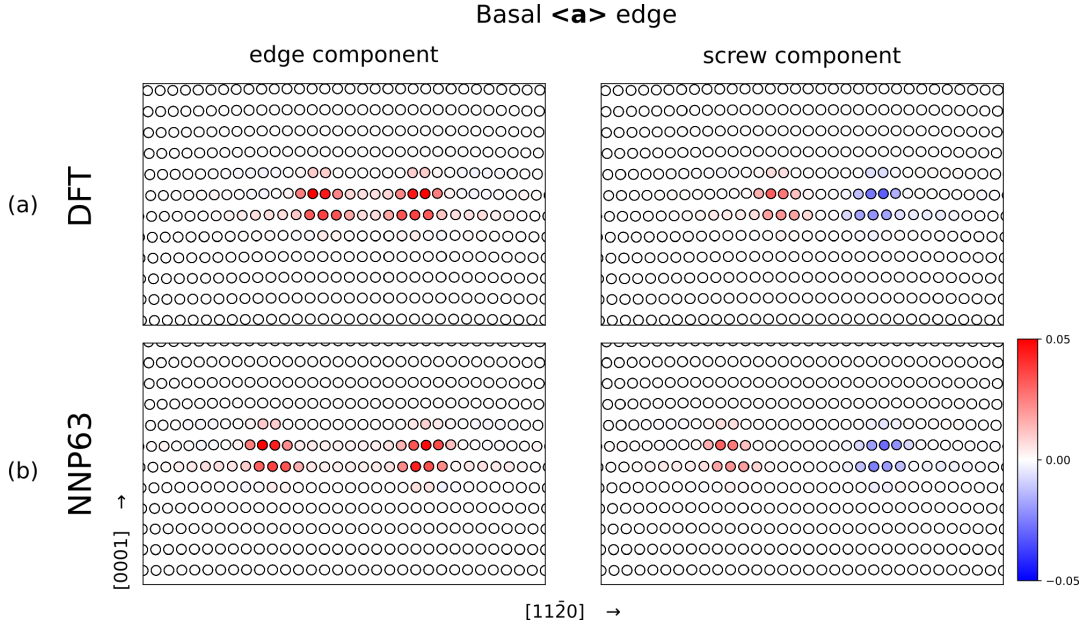


FIG. 6. Dissociated core structure of the basal $\langle \mathbf{a} \rangle$ edge dislocation with superimposed Nye tensor components of the edge (left column) and screw (right column) components from DFT (a) and NNP63 (b). DFT results in (a) are from [73].

528 For the basal $\langle \mathbf{a} \rangle$ edge dislocation in Figure 6 the Nye tensor components for NNP63
 529 agree extremely well with DFT for both edge and screw components. A summation of
 530 the edge component yields the exact Burgers vector, while a summation over the screw
 531 component results in zero, as required. Compared with DFT, NNP63 predicts a larger
 532 partial dislocation separation consistent with a combination of a slightly lower stable stacking
 533 fault energy and slightly higher elastic constants. The Nye tensor components for the basal
 534 $\langle \mathbf{a} \rangle$ screw dislocation are shown in Figure 7. As for the edge dislocation, the NNP63 core
 535 agrees very well with DFT. And as required, the edge components sum to zero and the
 536 screw components sum to the exact Burgers vector. A small difference is noticeable in the
 537 distribution. While there is no indication of partial dislocation separation for both cores,
 538 the Nye tensor components from NNP63 are slightly less compact than the reference DFT.
 539 Predictions of the core structure of the MEAM1 (not shown here) for the basal $\langle \mathbf{a} \rangle$

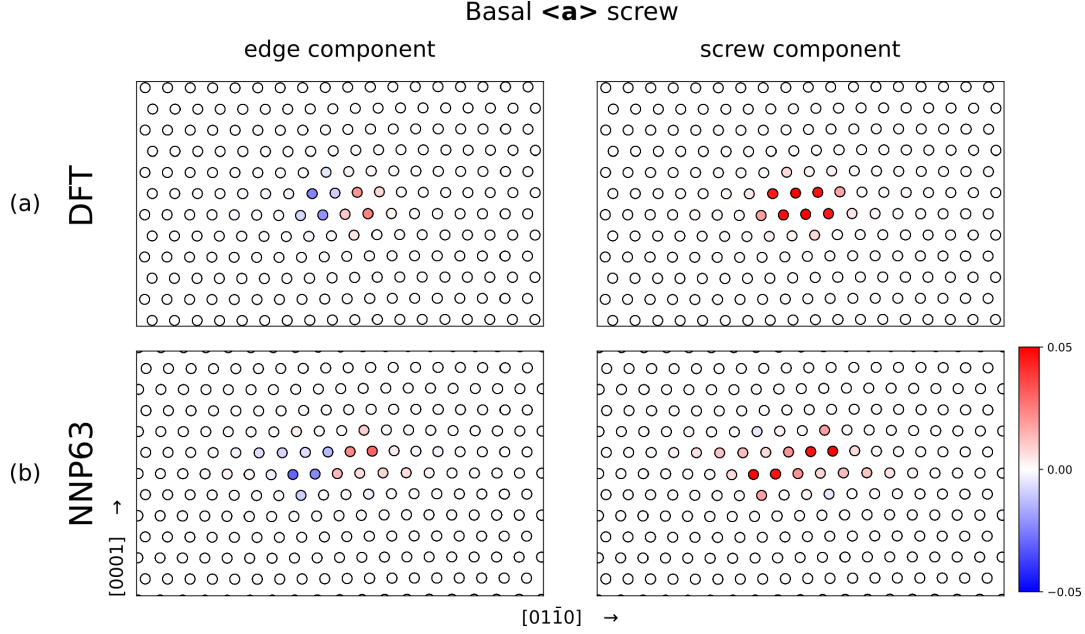


FIG. 7. Dissociated core structure of the basal $\langle \mathbf{a} \rangle$ screw dislocation with superimposed Nye tensor components of the edge (left column) and screw (right column) components from DFT (a) and NNP63 (b). DFT results in (a) are from [73].

540 dislocations compare less favorably to the DFT reference. While the partial dislocation
 541 structures are predicted well, both the edge and screw dislocation cores exhibit a much
 542 larger separation distance, see e.g. [5] for comparison, due to the large error in basal stable
 543 stacking fault energy.

544 We have also examined the Peierls stress of the basal $\langle \mathbf{a} \rangle$ edge dislocation. The basal
 545 $\langle \mathbf{a} \rangle$ dislocation is the prevalent system in pure Mg, with a very low Peierls stress that
 546 controls the measured yield strength in all but idealized crystal orientations. Using standard
 547 procedures, NNP63 exhibits a $T=0$ K Peierls stress of $\sigma_P \approx 0.05$ MPa for the basal edge
 548 dislocation. This is smaller than experiments (~ 0.5 MPa); other potentials show results
 549 higher than experiments, but all values remain quite small so that alloying to increase the
 550 basal strengthening is usually necessary for an engineering material.

551 Dislocations with $\langle \mathbf{c} + \mathbf{a} \rangle$ Burgers vector on the pyramidal I and II planes are important in
 552 Mg because they provide the accessible plastic slip in the $\langle \mathbf{c} \rangle$ axis direction. Figure 8 shows
 553 the Nye tensor analysis for the pyr.II edge core from DFT and NNP63. The pyr.II edge
 554 core is relevant for investigating solute strengthening effects [74, 75]. Dissociation is clearly
 555 along a pyramidal II plane. Comparing the Nye components of the two partial cores yields

556 a very good match between DFT and NNP63. The edge components match especially well
 557 while the screw components are smaller and agree slightly less well. The partial dislocation
 558 separation is slightly larger for the NNP63 prediction, again in line with the slightly smaller
 559 stacking fault energy.

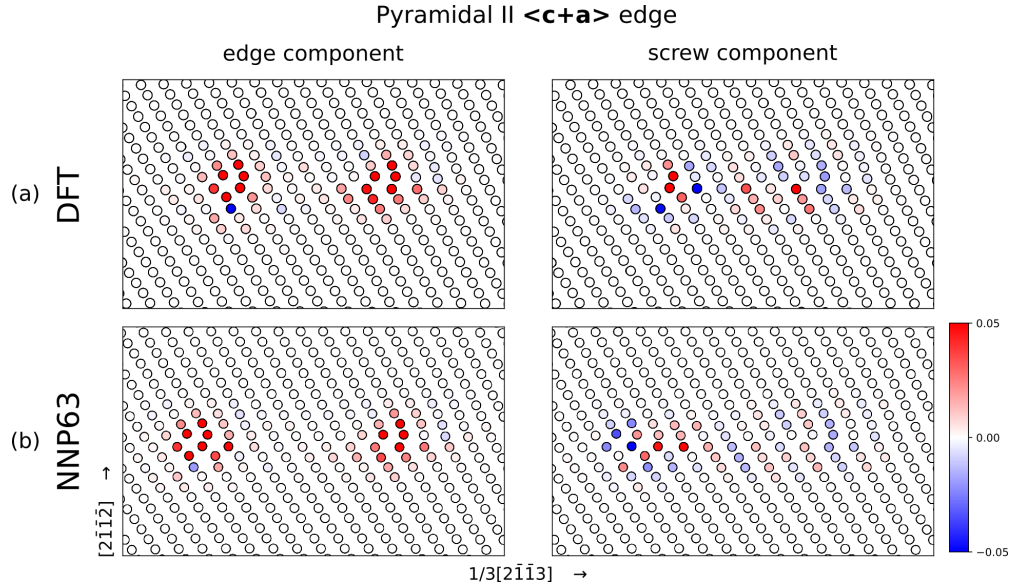


FIG. 8. Dissociated core structures of the pyramidal II $\langle \mathbf{c} + \mathbf{a} \rangle$ edge dislocations with superimposed Nye tensor components of the edge (left column) and screw (right column) components; (a) DFT from [74]; (b) NNP63.

560 Of perhaps most importance for the $\langle \mathbf{c} + \mathbf{a} \rangle$ Burgers vector dislocations is the the energy
 561 difference $\Delta E_{\text{I-II}} = \Delta E_{\text{I}} - \Delta E_{\text{II}}$ between pyr.I and II screw dislocations, where a positive
 562 value indicates that pyr. II is more stable (lower energy). This energy difference has been
 563 identified as the key material parameter for ductility in Mg due to its role in controlling a
 564 cross-slip process that enables significant $\langle \mathbf{c} + \mathbf{a} \rangle$ slip [35]. However, this energy difference is
 565 very small and so is not well-established in DFT itself. Using a quadrupolar DFT cell [76]
 566 reported an energy difference of $\Delta E_{\text{I-II}} = 7 \pm 20$ meV/nm (pyr. II more stable); the small cell
 567 size and periodic boundary conditions can have a non-negligible effect on the total energy,
 568 however. We have performed DFT using a very large (up to 2000 atoms) cylindrical geometry
 569 with outer boundaries fixed at the anisotropic elastic displacement field for a Volterra $\langle \mathbf{c} + \mathbf{a} \rangle$
 570 screw dislocation using the DFT lattice and elastic constants. We find that the sign of the
 571 energy difference varies with increasing cell radius, with $\Delta E_{\text{I-II}} = -30$ meV/nm at the
 572 largest size (pyr. I favorable, in conflict with experiments). So, even DFT is uncertain here,

573 and the NNP is trained only on DFT structures that do not include actual dislocations.
574 Additional complexity related to the pyramidal slip systems arise during the stable stacking
575 fault calculations during which complex shuffling processes are observed which lead to a
576 lower energy, see [55], with the actual stable fault positions and energies marked with x's
577 in Figure 5 in the pyr.II GSFE. Actual dislocations are even more complex in geometry
578 and might include further shuffling processes during relaxation that are not present in the
579 training dataset by design and hence are probably not fully captured by the NNPs or any
580 other potential.

581 With the above background, Figures 9a, b show the screw dislocation core structures
582 for the pyr.I dislocation with the edge and screw Nye tensor components superimposed as
583 obtained from our DFT calculation (noting that the structure is quite robust with respect
584 to cell size) and as predicted by NNP63. Both cores are split into two partial dislocations
585 and the partial cores show a very good agreement: large screw components and small edge
586 components. A summation of the screw components yields the expected Burgers vector, and
587 the summation over the edge components is zero. The screw components show a dissociation
588 along the pyr.I plane with a short section along the pyr.II plane. The relative positions of
589 the partial dislocations differ slightly. The segment along the pyr.II plane is slightly longer
590 for the DFT geometry, which results in the right partial dislocation being two pyr.I planes
591 below the left partial as opposed to just one for the NNP63 geometry. Overall, the level of
592 agreement for this complex defect is good.

593 Figures 9c, d show the structure and Nye tensor components for the pyramidal II screw
594 dislocation from DFT and NNP63, respectively. The DFT results are re-analyzed from [77].
595 The partial separation distance is similar but there are notable differences in structure. Most
596 importantly, the DFT core structure shows a dissociation in the pyramidal II plane while
597 the NNP63 core shows what appears to be some dissociation on the pyramidal I plane. That
598 is, the left and right partials in Figure 9d are not similar, with the left partial of the NNP63
599 geometry extending further along a pyr.I plane. This quasi-mixed pyr.II – pyr.I structure
600 obtained for the NNP63 pyr.II core presumably reflects the delicate energetic competition
601 between pyr.II and pyr.I cores, which NNP63 is not able to fully resolve. The pyr.II core as
602 predicted by the MEAM1 (not shown), on the other hand, does show dissociation only on
603 the pyr.II plane (cf. [6]) and so its structure is in better agreement with DFT. However, the
604 pyr.II core as predicted by the MEAM2 potential bears some similarity to that predicted

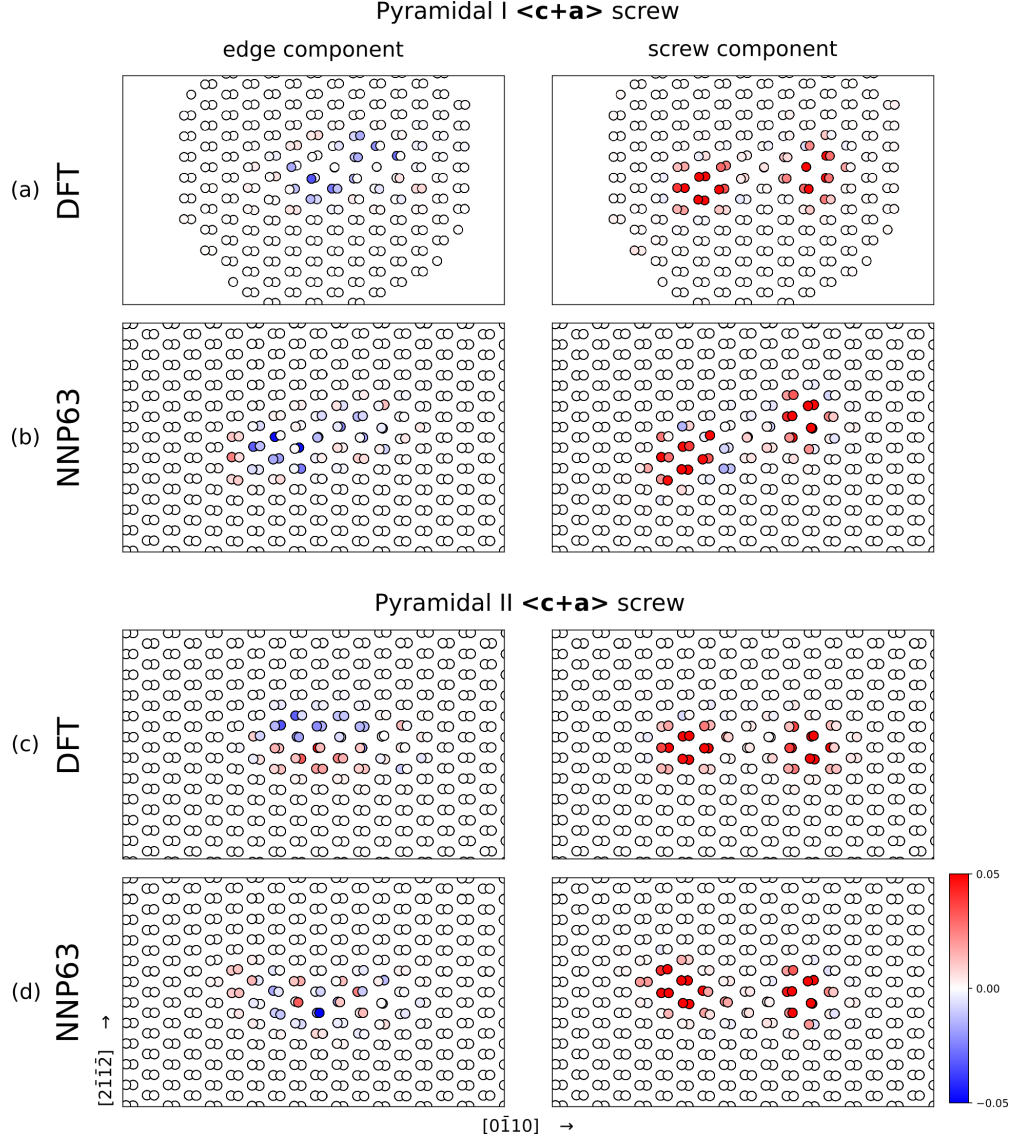


FIG. 9. Dissociated core structure of the pyramidal I and II $\langle \mathbf{c} + \mathbf{a} \rangle$ screw dislocation with superimposed Nye tensor components of the edge (left column) and screw (right column) components; (a) pyramidal I core from DFT; (b) NNP63 pyramidal I core; (c) pyramidal II core from DFT and (d) the NNP63 prediction. The missing atoms in subfigure (a) are related to the procedure in DFT; the reader is referred to the text for an explanation. Results for the pyramidal II in (b) from DFT are replotted from [74]. DFT geometries for pyramidal I in figure (a) are own results.

605 by NNP63, i.e. the left partial extends slightly along the pyr. I plane, and the right partial
 606 is in less-good agreement with DFT. Thus, the possible error in structure for NNP63 may
 607 not be unique to the type of potential.

608 The key pyr. I-II energy difference $\Delta E_{\text{I-II}}$ varies with the potential. The MEAM1 po-

609 tential predicts an energy difference of $\Delta E_{\text{I-II}} = 27 \text{ meV/nm}$ while the MEAM2 potential
610 gives an energy difference of $\Delta E_{\text{I-II}} = 54 \text{ meV/nm}$ (pyr. II stable for both, consistent with
611 experiments). Another version of the MEAM2 was developed to make pyr. I energetically
612 favorable with $\Delta E_{\text{I-II}} = -28 \text{ meV/nm}$ with negligible changes to other properties [6]. Both
613 the uncertainty in the DFT studies and the fact that the MEAM can be tweaked to change
614 the absolute stability of pyr. I vs. pyr. II is an indication that the energy balance is very
615 subtle. The NNP63 potential based solely on DFT inputs predicts a pyr. I-II energy differ-
616 ence of 170 meV/nm so that pyr. II is much more stable than obtained by other estimates.
617 This is in spite of the observation that the relaxed pyr. II structure appears to be a mix of
618 a pyr. II-like partial and a pyr. I-like partial. Limited tests with other NNPs show similar
619 dislocation cores and energy differences.

620 The procedure to obtain the pyr. I dislocation screw core by the annealing process de-
621 scribed earlier yields many screw dislocation cores in pyramidal I and II planes as well as
622 the mixed type in the case of NNP63. Their structures are generally very similar with unde-
623 tectable differences but exhibit differences in energy. Those energy differences are presented
624 in Figure 10 for NNP63 and both MEAMs. The reference energy for NNP63 is the energy
625 corresponding to the mixed-type pyr. II structure presented in Figure 9d. The references
626 for the two MEAMs are the pyr. II dislocation cores. Nearly all of the cores created with
627 NNP63 are found to be either identical to, or mostly less than $\sim 10 \text{ meV/nm}$ above, the
628 lowest-energy structure. The energies cluster into just a few distinct values. One structure
629 had an energy $\approx 170 \text{ meV/nm}$ that is close to the pyr. I screw energy, and one structure had
630 an energy $\approx 125 \text{ meV/nm}$. Overall, however, and unlike assumptions that ML potentials
631 may have many local spurious minima, NNP63 is quite robust for this defect. In contrast,
632 the energy differences among the MEAMs are much more widely distributed, with a range
633 of distinct energies spanning up to $\approx 70 \text{ meV/nm}$ for the MEAM1 and $\approx 50 \text{ meV/nm}$ for the
634 MEAM2, but with some structures with even higher energies extending up to the maximum
635 found for NNP63. Thus, it is actually the MEAM potentials that have many metastable
636 structures for this complex defect.

637 Overall, there is currently no resolution of the pyr. I-II screw competition based on any
638 computational method (DFT, NNP, MEAM). This problem thus requires considerably more
639 study at the first-principles level. The apparent mixed structure of the pyr. II screw core
640 as predicted by NNP63 makes it of questionable use for studies involving this dislocation.

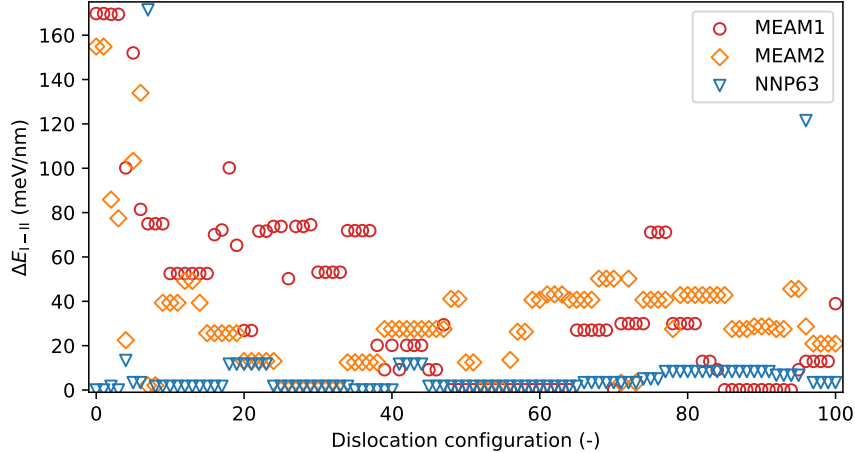


FIG. 10. Energy differences to pyr.II cores for various relaxed screw dislocation geometries in on pyramidal planes from the two MEAMs and NNP63.

641 Limited studies with other NNPs in our family of 129 potentials also do not exhibit a clear
 642 pyramidal II core dissociation with the described procedure. This remains an issue for
 643 further study and resolution.

644 In summary, even though dislocation geometries were not part of the training dataset,
 645 the NNP63 generally reproduces well the various dislocation geometries and Burgers vector
 646 distributions found in DFT studies. The Peierls stresses for basal and prism $\langle \mathbf{a} \rangle$ are also in
 647 reasonable agreement with experiments. Only the pyramidal II screw dislocation shows a
 648 different behavior that may be related to the inability of NNP63 to capture the (uncertain,
 649 even in DFT) energy differences between the pyr.I and II partial dislocations. While we are
 650 able to compare to available DFT studies, such studies are very computationally intensive,
 651 and are not at all feasible for properties beyond the basic structure of a straight periodic
 652 dislocation line with high-symmetry character (e.g. edge or screw). The success here of the
 653 NNP opens up the study of many other plasticity phenomena at metallurgically-relevant
 654 length and time scales.

655 D. Fracture: decohesion and intrinsic ductility

656 Fracture is a complex process involving very high multiaxial stresses around the crack
 657 tip with atomistic regions spanning from fully-decohered to moderately-deformed perfect
 658 crystals. Capturing proper fracture behavior, and even simply avoiding totally unphysical

659 behavior at the crack tip, represents a high challenge for any interatomic potential. Various
 660 physically-motivated potentials (EAM [64], MEAM [78], Stillinger-Weber [79], etc.) and the
 661 machine learning GAP Fe potential [24] all give unphysical crack tip behavior in spite of
 662 making good predictions for many other material properties and defects. Fracture is thus a
 663 very demanding test for any interatomic potential.

664 Moreover, the precise behavior at a crack tip determines whether a material is intrinsically
 665 brittle or intrinsically ductile. An intrinsically brittle material will cleave and create new
 666 surfaces. An intrinsically ductile material will emit dislocations, blunting the crack and
 667 preventing the brittle cleavage failure. It is computationally prohibitive to study cracks
 668 accurately with DFT because large sizes are needed, the geometry is non-periodic, and many
 669 load levels are needed to find the cleavage or emission load. Limited studies to date have
 670 thus relied on multiscale methods [80–84]. This makes the framework of anisotropic Linear
 671 Elastic Fracture Mechanics (LEFM) valuable for predicting both cleavage and dislocation
 672 emission. For Mg in particular, the cleavage and emission phenomena are predicted to occur
 673 at nearly the same load levels for a number of crack orientations, making it a particularly
 674 sensitive case. Modeling fracture behavior in Mg and Mg alloys thus again requires highly
 675 accurate interatomic potentials.

676 Fracture in Mode I (tensile) loading is controlled by the stress intensity factor K_I , which is
 677 the strength of the square-root singularity in the crack tip stress field. The thermodynamic
 678 critical stress intensity factor for cleavage in mode I for an atomically sharp crack is given
 679 by [85]:

$$K_{Ic} = \sqrt{\frac{2\gamma_s}{\Lambda_{22}}}, \quad (8)$$

680 where γ_s is the surface energy and Λ is an elasticity parameter [86]. A critical stress
 681 intensity for dislocation emission in Mode I cannot be determined exactly, but has been
 682 accurately estimated as [87, 88]

$$K_{Ie} = \sqrt{G_{Ie}^{\text{first}}(\theta, \varphi_{\text{first}}) o(\theta, \varphi)} / |F_{12}(\theta)| \quad \text{with} \quad (9)$$

$$G_{Ie}^{\text{first}} = \begin{cases} 0.145 \gamma_s^e + 0.5 \gamma_{\text{usf}}^e & , \gamma_s^e > 3.45 \gamma_{\text{usf}}^e \\ \gamma_{\text{usf}}^e & , \text{otherwise,} \end{cases} \quad (10)$$

683 where γ_s^e and γ_{usf}^e are the surface energy and unstable stacking fault energy of the emission
 684 plane, respectively; σ is an anisotropic elastic coefficient, θ and φ are the inclinations of the
 685 slip plane and Burgers vectors, F_{ij} is the resolved applied K field to an effective shear along
 686 the dislocation slip plane, and indices 1 and 2 refer to the crack growth direction and normal
 687 to the crack plane, respectively [89]. The LFM analysis thus shows that the critical material
 688 parameters for assessing cleavage and emission are the surface energies, the unstable stacking
 689 fault energies, and the elastic constants (which enter both phenomena, so differences mainly
 690 depend on the anisotropy, not the absolute values). With this background, we note that we
 691 have already examined the predictions of NNP63 for the elastic constants, surface energies,
 692 and unstable stacking fault energies. NNP63 provides much better accuracy for the surface
 693 energies as compared to both MEAM1 and MEAM2, and is better than MEAM1 for the
 694 unstable stacking fault energies. Since the intrinsic ductility depends on both quantities, we
 695 can expect NNP63 to be more realistic for assessing the fracture behavior of Mg.

696 Before examining atomistic crack tips, we first study the atomistic decohesion energy, i.e.
 697 the energy versus separation distance for rigid separation of two blocks of material across
 698 specified surface. This decohesion curve is the “cohesive zone” that determines the crack tip
 699 shape during loading [90]. Figure 11 shows the decohesion energy versus normal separation
 700 distance as computed via DFT, NNP63, and the two MEAMs for the basal, prismatic, pyra-
 701 midal I, and pyramidal II planes. The DFT data was contained in the training set but here,
 702 for clarity, not all data points are shown. The energy at maximum separation is twice the
 703 unrelaxed surface energy, and shows deviations for the MEAM potentials that are compa-
 704 rable to the deviations found for the fully-relaxed surfaces (Table I). In contrast, results for
 705 NNP63 generally agree better with DFT except for basal decohesion. The maximum cohe-
 706 sive stress corresponds to the maximum slope in the decohesion curve, and is well-captured
 707 by all potentials except for the MEAM potentials under basal separation. NNP63 shows
 708 a small maximum in the energy prior to full separation. This is unphysical; beyond this
 709 maximum, the surfaces are being pushed apart rather than pulled together. However, the
 710 effect is small and does not have broader significance.

711 We now examine the phenomena occurring at the tip of a sharp crack via simulation. In
 712 this study, we assess the whether the NNP gives physical behavior and, if so, whether or not
 713 the intrinsic ductility of Mg for relevant fracture orientations is consistent with theoretical
 714 predictions. We use the semi-infinite crack “K-test” for high accuracy [89] with an atomistic

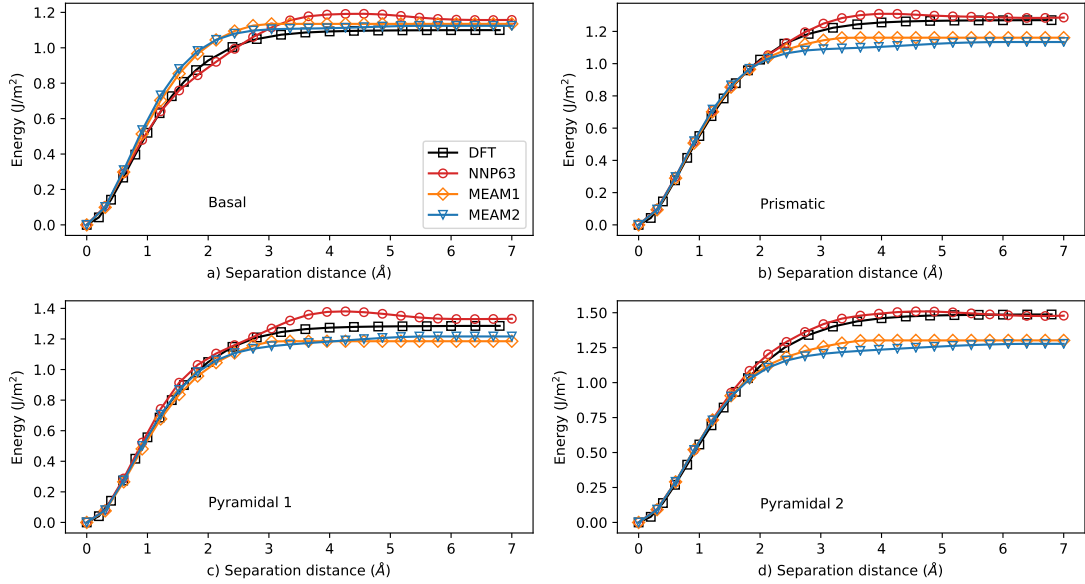


FIG. 11. Decoherence curves for basal, prism, pyramidal I and pyramidal II planes; comparison between DFT, NNP63 and the two MEAM potentials. All DFT data points are part of the training set.

715 domain size of $L_x = 500$ nm, $L_y = 500$ nm, and $L_z = 10$ nm with x the crack growth
716 direction, y the normal to the crack plane, and z the crack line direction with periodicity
717 imposed in this direction. The theoretical critical values of K_{Ic} and K_{Ie} are computed, and
718 all atoms are displaced according to the anisotropic K-field solution at a value of K_I just
719 below the lower of the two critical values. Atoms within $\sim 2r_c$ of the outer $x - y$ boundaries
720 are held fixed and the energy is then minimized by relaxing all interior atoms. Increments
721 in K_I are then imposed until some simulated critical value is reached at which the system
722 undergoes either a cleavage or emission event. As a first result, no anomalous or unphysical
723 behavior is observed for any crack geometry when using NNP63; this is already a very
724 positive result.

725 Table II shows the predicted and observed results obtained using NNP63. In all cases, the
726 observed/simulated behavior coincides with the predicted behavior using the DFT material
727 properties, cf. Table V. The simulated and predicted critical values differ slightly, but this is
728 typical due to the well-known existence of lattice trapping for cleavage fracture and the non-
729 exact (although generally quite accurate) theory for emission. The only notable quantitative
730 deviation between simulation and theory is for the pyramidal II orientation case where the

731 simulated emission occurs at $0.82 K_{\text{Ic}}^{\text{th}}$, i.e. much lower than the theoretical value. NNP63
 732 thus provides very good predictions for all fracture orientations studied.

TABLE II. Stress intensity factors K_{I} for cleavage and emission for various crack orientations as computed and simulated using NNP63 and its material properties. The observed events using the MEAM1 potential are also shown [91]. Critical K values in boldface indicate the predicted event. Cases where the MEAM1 event differs from the NNP63-observed and DFT-predicted event are indicated in italics.

Crack plane	Predicted critical K and event			Observed NNP63		NNP63 vs. Pred	MEAM1
	$K_{\text{Ic}}^{\text{th}}$	$K_{\text{Ie}}^{\text{th}}$	event	K	event	$K^{\text{NNP}}/K^{\text{pred}}$	event [91]
Basal I	0.265	0.284	cleavage	0.280	cleavage	1.06	cleavage
Basal II	0.265	0.291	cleavage	0.263	cleavage	0.99	cleavage
Prismatic I	0.297	0.253	emission	0.236	emission	0.93	<i>cleavage</i>
Prismatic II	0.307	0.282	emission	0.283	emission	1.00	<i>cleavage</i>
Pyramidal I	0.284	0.237	emission	0.250	emission	1.05	emission
Pyramidal II	0.302	0.286	emission	0.220	emission	0.82	<i>cleavage</i>

733 Table II also shows the events obtained from MEAM1 simulations as reported previ-
 734 ously [91]. While simulations using MEAM1 agree with theoretical predictions using the
 735 material properties of MEAM1 [91] (not shown here), the operative MEAM1 event differs
 736 from the NNP63 event for some orientations while the NNP63 event agrees with the event
 737 predicted using DFT material properties. Specifically, the MEAM1 predicts three orien-
 738 tations (prismatic I, II and pyramidal II) to be brittle (cleavage) whereas NNP63 predicts
 739 them all to be ductile (emission).

740 Figure 12 shows the geometries and structures after these events, highlighting the funda-
 741 mentally different physically behavior. These differences are important because they indicate
 742 that Mg is not as brittle as suggested by studies based on the MEAM1 potential. The differ-
 743 ence in phenomenon is directly traceable to the differences in underlying material properties.
 744 The MEAM1 potential provides poorer predictions of the surface and/or unstable stacking
 745 fault energies as compared to the NNP63 potential, and this leads to different behavior in
 746 simulations. Furthermore, while both potentials predict the basal orientation to be brittle,
 747 NNP63 predicts a much closer competition, with $K_{\text{Ie}}^{\text{th}}/K_{\text{Ic}}^{\text{th}} \approx 0.93$ for NNP63 as compared
 748 to ≈ 0.73 for MEAM1 [91]. This suggests the possibility that dilute alloying could have a

749 more important effect in changing the brittle basal behavior than obtained by recent studies
 750 on a model Mg-Y alloy using an alloy MEAM potential [91].

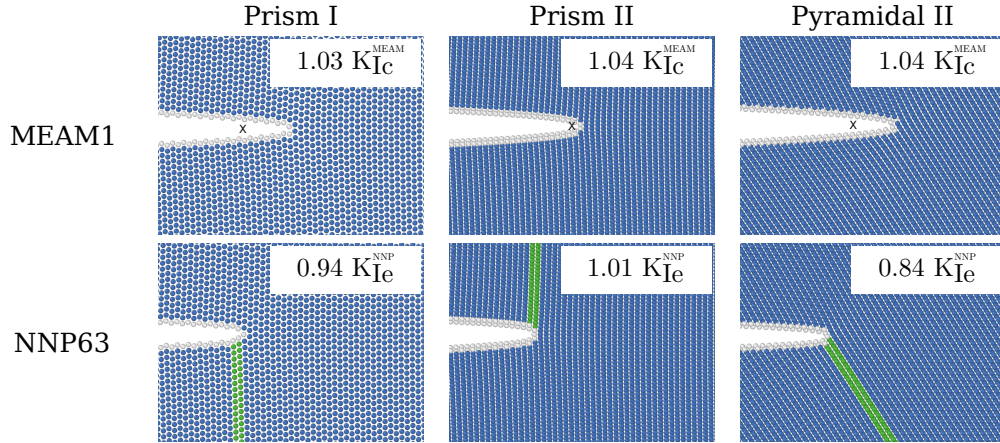


FIG. 12. Cross sectional view of crack tips post fracture for prismatic I, prismatic II, and pyramidal II crack planes, as observed in simulations for the MEAM1 and NNP63. The corresponding K values at each event are shown relative to K_{Ic} for the MEAM and K_{Ic} for NNP63 in the respective crack plane. Visualization used the Common Neighbor Analysis [71] (blue = hcp, green = fcc, gray = other) and the black “x” denotes the initial crack position for cleavage events.

751 IV. DISCUSSION

752 We have presented a neural network interatomic potential for Magnesium using the
 753 Behler-Parrinello symmetry functions for the description of the atomic environments within
 754 the n2p2 [38] framework. Magnesium has been studied due to (i) its important technological
 755 value, (ii) the complexities associated with dislocations and slip in the hcp crystal structure,
 756 (iii) the close competition between intrinsic brittleness and intrinsic ductility, and (iv) the
 757 need to understand the atomistic mechanisms that enhance the performance of dilute Mg al-
 758 loys relative to pure Mg, which will require interatomic potentials for complex alloy systems.
 759 Compared to existing very good MEAM potentials, NNP63 generally performs better for
 760 many material properties and crystalline defects that are critical to mechanical performance.
 761 These improvements were accomplished with a rather small DFT training dataset, extended
 762 only beyond a relatively standard set of structures to enable accurate fracture modeling. The
 763 addition of further selected data to improve on specific defect properties (as was done here

764 for fracture) is easily accomplished within the parameter-rich NNP framework. Because the
765 NNP formalism is regression, extrapolations could be highly inaccurate, and so the present
766 potential was carefully assessed in many scenarios relevant for plasticity and fracture.

767 The current potential remains less than ideal for the pyramidal II screw dislocation struc-
768 ture. The important pyr. I-II screw energy difference will likely require improvements as well.
769 However, accurate DFT reference data is not yet available, and may remain challenging due
770 to the very small energy difference. The Mg potential NNP63 was also not tested for grain
771 boundary structures or interstitial atoms, and so is not yet a fully-general potential for Mg.
772 Nonetheless, the delicate tension twin boundary energy (and structure) is well-predicted
773 although not in the training set. Both the vacancy formation and migration energies are
774 also in good agreement with DFT while, along with the dislocation and crack structures,
775 not being in the training data set. The melting point of NNP63 is also in good agreement
776 with experiments. These results are encouraging not only for Mg but also for the broader
777 prospects for machine learning potentials.

778 The present well-converged and consistent DFT training set developed here is openly
779 available [44]. This enables its application to other machine-learning methods and/or other
780 optimization functions that might better handle the structurally inhomogeneous datasets
781 typical for metallurgical applications. In particular, it would be valuable to develop a loss
782 function that is formulated in terms of energy differences between structures, rather than
783 absolute energies of individual structures. In any case, the quality of a potential for metal-
784 lurgical applications must not only be measured by the RMSE. Substantial tests outside of
785 the training dataset and/or to challenging but realistic structures (e.g. dislocations, crack
786 tips) must be included. The performance comes at a cost. Compared to the MEAM for-
787 malism as implemented in LAMMPS the n2p2 implementation [38] for BPNNs is 10× more
788 expensive computationally. Adding more elements to create interatomic potentials for alloys
789 increases the cost significantly [1]. However, if the aim of atomistic studies is to be quanti-
790 tatively correct for specific alloy compositions, then it is likely that only machine-learning
791 methods will provide an accuracy approaching that of DFT while at a tiny fraction of the
792 computational cost, even if this cost significantly exceeds that of traditional potentials.

793 Finally, although the potential presented here is not a general purpose Mg potential, this
794 work is among the first to demonstrate the broad application of a machine learned potential
795 to a cross-section of metallurgically-relevant properties, structures, and behaviors. NNP63

796 clearly improves upon existing traditional potentials that have been highly optimized, and
797 that are quantitatively among the best potentials among all those developed to date for pure
798 metals. This work sets the baseline for extensions to Mg alloys, which are very challenging
799 for interatomic potentials having fixed functional forms and limited flexibility and yet are
800 essential for the technological application of lightweight Mg alloys in energy-efficient struc-
801 tural components. The present potential can be used to study other defect-related problems
802 in Mg which includes, e.g. the prismatic-basal cross-slip mechanism. This is beyond the
803 scope of the current paper and will be presented in future work.

804 **ACKNOWLEDGMENTS**

805 MS, BY and WAC acknowledge support by the NCCR MARVEL funded by the Swiss
806 National Science Foundation. We also acknowledge support for high-performance computing
807 provided by the Scientific IT and Application Support (SCITAS) at EPFL. EM acknowledges
808 support from the Swiss National Science Foundation through project 200021_18198/1. MS
809 thanks G. Imbalzano for providing the CURSEL algorithm, M. Ghazisaeidi for providing the
810 pyr. II dislocation core geometry from DFT and A. Jain for providing the vacancy migration
811 barriers.

812 **Appendix A: Symmetry function hyperparameters**

813 Symmetry function choice optimized with CUR decomposition as described in II.

TABLE III. Hyperparameters for the radial symmetry functions.

Type	η	r_2	r_c
2	2.630×10^{-2}	0.0	8.0
2	1.560×10^{-2}	0.0	8.0
2	2.630×10^{-2}	0.0	8.0
2	6.900×10^{-3}	0.0	1.200×10^1
2	4.420×10^{-2}	0.0	8.0
2	1.560×10^{-2}	0.0	8.0
2	7.430×10^{-2}	0.0	8.0
2	7.430×10^{-2}	0.0	8.0
2	4.420×10^{-2}	0.0	8.0
2	1.560×10^{-2}	0.0	8.0
2	1.117×10^{-1}	1.301×10^1	1.600×10^1
2	1.821×10^{-1}	5.657	8.0
2	4.420×10^{-2}	0.0	8.0
2	1.170×10^{-2}	0.0	1.200×10^1
2	1.081×10^{-1}	1.322×10^1	2.0×10^1
2	7.150×10^{-2}	1.626×10^1	2.0×10^1
2	9.110×10^{-2}	8.0	1.600×10^1
2	4.550×10^{-2}	1.131×10^1	1.600×10^1
2	1.166×10^{-1}	7.071	2.0×10^1
2	5.830×10^{-2}	1.0×10^1	2.0×10^1
2	2.910×10^{-2}	1.414×10^1	2.0×10^1
2	3.900×10^{-3}	0.0	1.600×10^1
2	2.500×10^{-3}	0.0	2.0×10^1
2	5.560×10^{-2}	0.0	1.200×10^1
2	8.700×10^{-3}	0.0	2.0×10^1
2	1.350×10^{-2}	0.0	1.600×10^1
2	1.960×10^{-2}	0.0	1.200×10^1

814 **Appendix B: Fracture behavior prediction for DFT**

815 The discussion of the predictions and observations in Table II include a reference to
816 the event prediction based on DFT values for unstable stacking fault energies and surface
817 energies. The values behind these predictions are given here in Table V.

818 The event prediction is based on the minimum between the stress intensity factor for

TABLE IV. Hyperparameters for the angular symmetry functions.

Type	η	λ	ζ	r_c
3	6.900×10^{-3}	1	1.0	1.200×10^1
3	6.900×10^{-3}	1	4.0	1.200×10^1
3	6.900×10^{-3}	-1	1.0	1.200×10^1
3	1.170×10^{-2}	1	1.0	1.200×10^1
3	1.560×10^{-2}	1	1.0	8.0

TABLE V. Stress intensity factors K_I for cleavage (*c*) and emission (*e*) with material properties from the DFT for the event prediction in Table II. DFT values are taken as presented here I; surface energy for the prismatic II plane is taken from [92].

Plane	K_{Ic}	K_{Ie}	event prediction
Basal I	0.242	0.255	cleavage
Basal II	0.242	0.264	cleavage
Prismatic I	0.255	0.229	emission
Prismatic II	0.273	0.253	emission
Pyramidal I	0.259	0.214	emission
Pyramidal II	0.277	0.241	emission

819 cleavage and emission $\min(K_{Ie}, K_{Ic})$ and is highlighted in the table in bold numbers.

-
- 820 [1] D. Marchand, A. Glensk, and W. Curtin, Machine learning for metallurgy I. neural network
821 potential for Al-Cu, in preparation (2020).
822 [2] X.-Y. Liu, J. B. Adams, F. Ercolessi, and J. A. Moriarty, EAM potential for magnesium from
823 quantum mechanical forces, Modelling and Simulation in Materials Science and Engineering
824 **4**, 293 (1996).

- 825 [3] D. Y. Sun, M. I. Mendeleev, C. A. Becker, K. Kudin, T. Haxhimali, M. Asta, J. J. Hoyt,
826 A. Karma, and D. J. Srolovitz, Crystal-melt interfacial free energies in hcp metals: A molecular
827 dynamics study of mg, *Phys. Rev. B* **73**, 024116 (2006).
- 828 [4] Y.-M. Kim, N. J. Kim, and B.-J. Lee, Atomistic modeling of pure mg and mg–al systems,
829 *Calphad* **33**, 650 (2009).
- 830 [5] Z. Wu, M. F. Francis, and W. A. Curtin, Magnesium interatomic potential for simulating
831 plasticity and fracture phenomena, *Modelling and Simulation in Materials Science and Engi-*
832 *neering* **23**, 015004 (2015).
- 833 [6] R. Ahmad, Z. Wu, and W. Curtin, Analysis of double cross-slip of pyramidal $\langle c+a \rangle$ screw
834 dislocations and implications for ductility in mg alloys, *Acta Materialia* **183**, 228 (2020).
- 835 [7] A. P. Bartók, R. Kondor, and G. Csányi, On representing chemical environments, *Phys. Rev.*
836 *B* **87**, 184115 (2013).
- 837 [8] J. Behler, Representing potential energy surfaces by high-dimensional neural network poten-
838 tials, *Journal of Physics: Condensed Matter* **26**, 183001 (2014).
- 839 [9] R. Kobayashi, D. Giofré, T. Junge, M. Ceriotti, and W. A. Curtin, Neural network potential
840 for al-mg-si alloys, *Phys. Rev. Materials* **1**, 053604 (2017).
- 841 [10] G. Pun, R. Batra, R. Ramprasad, and Y. Mishin, Physically-informed artificial neural networks
842 for atomistic modeling of materials, arXiv preprint arXiv:1808.01696 (2018).
- 843 [11] H. Wang, L. Zhang, J. Han, and W. E, Deepmd-kit: A deep learning package for many-body
844 potential energy representation and molecular dynamics, *Computer Physics Communications*
845 **228**, 178 (2018).
- 846 [12] D. Dickel, D. Francis, and C. Barrett, Neural network aided development of a semi-empirical
847 interatomic potential for titanium, *Computational Materials Science* **171**, 109157 (2020).
- 848 [13] J. Behler and M. Parrinello, Generalized neural-network representation of high-dimensional
849 potential-energy surfaces, *Phys. Rev. Lett.* **98**, 146401 (2007).
- 850 [14] D. Rogers and M. Hahn, Extended-connectivity fingerprints, *J. Chem. Inf. Model.* **50**, 742
851 (2010).
- 852 [15] G. Montavon, M. Rupp, V. Gobre, A. Vazquez-Mayagoitia, K. Hansen, A. Tkatchenko, K.-
853 R. Müller, and O. A. von Lilienfeld, Machine learning of molecular electronic properties in
854 chemical compound space, *New Journal of Physics* **15**, 095003 (2013).
- 855 [16] A. P. Bartók and G. Csányi, Gaussian approximation potentials: A brief tutorial introduction,

- 856 International Journal of Quantum Chemistry **115**, 1051 (2015).
- 857 [17] F. A. Faber, L. Hutchison, B. Huang, J. Gilmer, S. S. Schoenholz, G. E. Dahl, O. Vinyals,
858 S. Kearnes, P. F. Riley, and O. A. von Lilienfeld, Prediction errors of molecular machine
859 learning models lower than hybrid dft error, Journal of chemical theory and computation **13**,
860 5255 (2017).
- 861 [18] L. Zhang, D.-Y. Lin, H. Wang, R. Car, and W. E, Active learning of uniformly accurate
862 interatomic potentials for materials simulation, Phys. Rev. Materials **3**, 023804 (2019).
- 863 [19] N. Bernstein, G. Csányi, and V. L. Deringer, De novo exploration and self-guided learning of
864 potential-energy surfaces, npj Computational Materials **5**, 99 (2019).
- 865 [20] R. Jinnouchi, F. Karsai, and G. Kresse, On-the-fly machine learning force field generation:
866 Application to melting points, Phys. Rev. B **100**, 014105 (2019).
- 867 [21] G. P. Pun, R. Batra, R. Ramprasad, and Y. Mishin, Physically informed artificial neural
868 networks for atomistic modeling of materials, Nature communications **10**, 2339 (2019).
- 869 [22] Y. Zuo, C. Chen, X. Li, Z. Deng, Y. Chen, J. Behler, G. Csányi, A. V. Shapeev, A. P.
870 Thompson, M. A. Wood, and S. P. Ong, Performance and cost assessment of machine learning
871 interatomic potentials, J. Phys. Chem. A **124**, 731 (2020).
- 872 [23] G. Imbalzano, A. Anelli, D. Giofré, S. Klees, J. Behler, and M. Ceriotti, Automatic selection of
873 atomic fingerprints and reference configurations for machine-learning potentials, The Journal
874 of Chemical Physics **148**, 241730 (2018).
- 875 [24] D. Dragoni, T. D. Daff, G. Csányi, and N. Marzari, Achieving dft accuracy with a machine-
876 learning interatomic potential: Thermomechanics and defects in bcc ferromagnetic iron, Phys.
877 Rev. Materials **2**, 013808 (2018).
- 878 [25] W. J. Szlachta, A. P. Bartók, and G. Csányi, Accuracy and transferability of gaussian approx-
879 imation potential models for tungsten, Phys. Rev. B **90**, 104108 (2014).
- 880 [26] F. Maresca, D. Dragoni, G. Csányi, N. Marzari, and W. A. Curtin, Screw dislocation structure
881 and mobility in body centered cubic fe predicted by a gaussian approximation potential, npj
882 Computational Materials **4**, 69 (2018).
- 883 [27] B. Mordike and T. Ebert, Magnesium: Properties — applications — potential, Materials
884 Science and Engineering: A **302**, 37 (2001).
- 885 [28] H. Friedrich and S. Schumann, Research for a “new age of magnesium” in the automotive
886 industry, Journal of Materials Processing Technology **117**, 276 (2001), containing keynote

- 887 papers presented at the proceedings of THERMEC'2000, the International conference on
888 Processing and manufacturing of Advanced Materials.
- 889 [29] T. M. Pollock, Weight loss with magnesium alloys, *Science* **328**, 986 (2010).
- 890 [30] K. K. Turekian and K. H. Wedepohl, Distribution of the elements in some major units of the
891 earth's crust, *Geological Society of America Bulletin* **72**, 175 (1961).
- 892 [31] D. Hull and D. J. Bacon, *Introduction to dislocations*, 4th ed. (Elsevier, 2011).
- 893 [32] Z. Wu and W. Curtin, Brittle and ductile crack-tip behavior in magnesium, *Acta Materialia*
894 **88**, 1 (2015).
- 895 [33] B. Yin, Z. Wu, and W. Curtin, First-principles calculations of stacking fault energies in mg-y,
896 mg-al and mg-zn alloys and implications for $\langle c+a \rangle$ activity, *Acta Materialia* **136**, 249 (2017).
- 897 [34] Z. Wu, R. Ahmad, B. Yin, S. Sandlöbes, and W. A. Curtin, Mechanistic origin and prediction
898 of enhanced ductility in magnesium alloys, *Science* **359**, 447 (2018).
- 899 [35] R. Ahmad, B. Yin, Z. Wu, and W. Curtin, Designing high ductility in magnesium alloys, *Acta*
900 *Materialia* **172**, 161 (2019).
- 901 [36] T. Nogaret, W. Curtin, J. Yasi, L. Hector, and D. Trinkle, Atomistic study of edge and screw
902 $\langle c + a \rangle$ dislocations in magnesium, *Acta Materialia* **58**, 4332 (2010).
- 903 [37] R. Ahmad, S. Groh, M. Ghazisaeidi, and W. A. Curtin, Modified embedded-atom method
904 interatomic potential for mg-y alloys, *Modelling and Simulation in Materials Science and*
905 *Engineering* **26**, 065010 (2018).
- 906 [38] A. Singraber, J. Behler, and C. Dellago, Library-based lammmps implementation of high-
907 dimensional neural network potentials, *J. Chem. Theory Comput.* **15**, 1827 (2019).
- 908 [39] J. Behler, Constructing high-dimensional neural network potentials: A tutorial review, *Inter-*
909 *national Journal of Quantum Chemistry* **115**, 1032 (2015).
- 910 [40] A. Singraber, *Designing and training neural network potentials for molecular dynamics simu-*
911 *lations: Application to water and copper sulfide*, Ph.D. thesis, Universität Wien (2018).
- 912 [41] A. Singraber, T. Morawietz, J. Behler, and C. Dellago, Parallel multistream training of high-
913 dimensional neural network potentials, *J. Chem. Theory Comput.* **15**, 3075 (2019).
- 914 [42] S. Lorenz, A. Groß, and M. Scheffler, Representing high-dimensional potential-energy surfaces
915 for reactions at surfaces by neural networks, *Chemical Physics Letters* **395**, 210 (2004).
- 916 [43] J. B. Witkoskie and D. J. Doren, Neural network models of potential energy surfaces: Proto-
917 typical examples, *Journal of Chemical Theory and Computation* **1**, 14 (2005), pMID: 26641111.

- 918 [44] B. Yin, M. Stricker, and W. Curtin, Pure magnesium dft calculations for interatomic potential
919 fitting, materials cloud archive; draft, MaterialsCloud (2020).
- 920 [45] G. Kresse and J. Furthmüller, Efficient iterative schemes for ab initio total-energy calculations
921 using a plane-wave basis set, *Phys. Rev. B* **54**, 11169 (1996).
- 922 [46] G. Kresse and D. Joubert, From ultrasoft pseudopotentials to the projector augmented-wave
923 method, *Phys. Rev. B* **59**, 1758 (1999).
- 924 [47] J. P. Perdew, K. Burke, and M. Ernzerhof, Generalized gradient approximation made simple,
925 *Phys. Rev. Lett.* **77**, 3865 (1996).
- 926 [48] P. E. Blöchl, Projector augmented-wave method, *Phys. Rev. B* **50**, 17953 (1994).
- 927 [49] H. J. Monkhorst and J. D. Pack, Special points for brillouin-zone integrations, *Phys. Rev. B*
928 **13**, 5188 (1976).
- 929 [50] M. Methfessel and A. T. Paxton, High-precision sampling for brillouin-zone integration in
930 metals, *Phys. Rev. B* **40**, 3616 (1989).
- 931 [51] C. Barrett and T. Massalski, *Structure of Metals, International Series on Materials Science*
932 *and Technology*, 3rd ed. (Pergamon, 1980).
- 933 [52] S. Plimpton, Fast parallel algorithms for short-range molecular dynamics, *Journal of Compu-*
934 *tational Physics* **117**, 1 (1995).
- 935 [53] A. Stukowski, Visualization and analysis of atomistic simulation data with OVITO—the open
936 visualization tool, *Modelling and Simulation in Materials Science and Engineering* **18**, 015012
937 (2009).
- 938 [54] Z. Wu and W. A. Curtin, The origins of high hardening and low ductility in magnesium,
939 *Nature* **526**, 62 (2015).
- 940 [55] B. Yin, Z. Wu, and W. Curtin, Comprehensive first-principles study of stable stacking faults
941 in hcp metals, *Acta Materialia* **123**, 223 (2017).
- 942 [56] G. Walker and M. Marezio, Lattice parameters and zone overlap in solid solutions of lead in
943 magnesium, *Acta Metallurgica* **7**, 769 (1959).
- 944 [57] E. Wachowicz and A. Kiejna, Bulk and surface properties of hexagonal-close-packed be and
945 mg, *Journal of Physics: Condensed Matter* **13**, 10767 (2001).
- 946 [58] G. Simmons and H. Wang, *Single Crystal Elastic Constants and Calculated Aggregate Prop-*
947 *erties. A Handbook*, 2nd ed. (Cambridge, MA: MIT Press, 1971).
- 948 [59] J. Han, X. Su, Z.-H. Jin, and Y. Zhu, Basal-plane stacking-fault energies of mg: A first-

- 949 principles study of li- and al-alloying effects, *Scripta Materialia* **64**, 693 (2011).
- 950 [60] Z. Pei, X. Zhang, T. Hickel, M. Friák, S. Sandlöbes, B. Dutta, and J. Neugebauer, Atomic
951 structures of twin boundaries in hexagonal close-packed metallic crystals with particular focus
952 on mg, *npj Computational Materials* **3**, 6 (2017).
- 953 [61] P. Tzanetakis, J. Hillairet, and G. Revel, The formation energy of vacancies in aluminium and
954 magnesium, *physica status solidi (b)* **75**, 433 (1976).
- 955 [62] F. Musil, M. J. Willatt, M. A. Langovoy, and M. Ceriotti, Fast and accurate uncertainty
956 estimation in chemical machine learning, *J. Chem. Theory Comput.* **15**, 906 (2019).
- 957 [63] M. S. Daw and M. I. Baskes, Semiempirical, quantum mechanical calculation of hydrogen
958 embrittlement in metals, *Phys. Rev. Lett.* **50**, 1285 (1983).
- 959 [64] M. S. Daw and M. I. Baskes, Embedded-atom method: Derivation and application to impu-
960 rities, surfaces, and other defects in metals, *Phys. Rev. B* **29**, 6443 (1984).
- 961 [65] P. M. Morse, Diatomic molecules according to the wave mechanics. ii. vibrational levels, *Phys.*
962 *Rev.* **34**, 57 (1929).
- 963 [66] E. J. Ragasa, C. J. O'Brien, R. G. Hennig, S. M. Foiles, and S. R. Phillpot, Multi-objective
964 optimization of interatomic potentials with application to MgO, *Modelling and Simulation in*
965 *Materials Science and Engineering* **27**, 074007 (2019).
- 966 [67] I. Shin and E. A. Carter, Simulations of dislocation mobility in magnesium from first principles,
967 *International Journal of Plasticity* **60**, 58 (2014).
- 968 [68] atomman: <https://github.com/usnistgov/atomman> (2020).
- 969 [69] C. Hartley and Y. Mishin, Characterization and visualization of the lattice misfit associated
970 with dislocation cores, *Acta Materialia* **53**, 1313 (2005).
- 971 [70] V. Vitek, R. C. Perrin, and D. K. Bowen, The core structure of $\frac{1}{2}(111)$ screw dislocations
972 in b.c.c. crystals, *The Philosophical Magazine: A Journal of Theoretical Experimental and*
973 *Applied Physics* **21**, 1049 (1970).
- 974 [71] D. Faken and H. Jónsson, Systematic analysis of local atomic structure combined with 3d
975 computer graphics, *Computational Materials Science* **2**, 279 (1994).
- 976 [72] A. Stukowski and K. Albe, Extracting dislocations and non-dislocation crystal defects from
977 atomistic simulation data, *Modelling and Simulation in Materials Science and Engineering*
978 **18**, 085001 (2010).
- 979 [73] J. A. Yasi, T. Nogaret, D. R. Trinkle, Y. Qi, L. G. Hector, and W. A. Curtin, Basal and prism

- 980 dislocation cores in magnesium: comparison of first-principles and embedded-atom-potential
981 methods predictions, *Modelling and Simulation in Materials Science and Engineering* **17**,
982 055012 (2009).
- 983 [74] M. Ghazisaeidi, L. Hector, and W. Curtin, First-principles core structures of $\{c+a\}$ edge and
984 screw dislocations in mg, *Scripta Materialia* **75**, 42 (2014).
- 985 [75] R. Ahmad, Z. Wu, S. Groh, and W. Curtin, Pyramidal $\{111\}$ to basal transformation of $\{c+a\}$
986 edge dislocations in mg-y alloys, *Scripta Materialia* **155**, 114 (2018).
- 987 [76] M. Itakura, H. Kaburaki, M. Yamaguchi, and T. Tsuru, Novel cross-slip mechanism of pyra-
988 midal screw dislocations in magnesium, *Phys. Rev. Lett.* **116**, 225501 (2016).
- 989 [77] M. Ghazisaeidi, L. Hector, and W. Curtin, Solute strengthening of twinning dislocations in
990 mg alloys, *Acta Materialia* **80**, 278 (2014).
- 991 [78] M. I. Baskes, Modified embedded-atom potentials for cubic materials and impurities, *Phys.*
992 *Rev. B* **46**, 2727 (1992).
- 993 [79] F. H. Stillinger and T. A. Weber, Computer simulation of local order in condensed phases of
994 silicon, *Phys. Rev. B* **31**, 5262 (1985).
- 995 [80] G. Lu, E. B. Tadmor, and E. Kaxiras, From electrons to finite elements: A concurrent multi-
996 scale approach for metals, *Phys. Rev. B* **73**, 024108 (2006).
- 997 [81] D. H. Warner, W. A. Curtin, and S. Qu, Rate dependence of crack-tip processes predicts
998 twinning trends in f.c.c. metals, *Nature Materials* **6**, 876 (2007).
- 999 [82] D. Warner and W. Curtin, Origins and implications of temperature-dependent activation
1000 energy barriers for dislocation nucleation in face-centered cubic metals, *Acta Materialia* **57**,
1001 4267 (2009).
- 1002 [83] X. Zhang, G. Lu, and W. A. Curtin, Multiscale quantum/atomistic coupling using constrained
1003 density functional theory, *Phys. Rev. B* **87**, 054113 (2013).
- 1004 [84] V. Yamakov, D. Warner, R. Zamora, E. Saether, W. Curtin, and E. Glaessgen, Investigation
1005 of crack tip dislocation emission in aluminum using multiscale molecular dynamics simulation
1006 and continuum modeling, *Journal of the Mechanics and Physics of Solids* **65**, 35 (2014).
- 1007 [85] A. A. Griffith, Vi. the phenomena of rupture and flow in solids, *Philosophical transactions of*
1008 *the royal society of london. Series A, containing papers of a mathematical or physical character*
1009 **221**, 163 (1921).
- 1010 [86] T. T. C. Ting, *Anisotropic Elasticity: Theory and Applications* (Oxford University Press,

- 1011 1996).
- 1012 [87] J. R. Rice, Dislocation nucleation from a crack tip: An analysis based on the peierls concept,
1013 Journal of the Mechanics and Physics of Solids **40**, 239 (1992).
- 1014 [88] P. Andric and W. Curtin, New theory for mode i crack-tip dislocation emission, Journal of
1015 the Mechanics and Physics of Solids **106**, 315 (2017).
- 1016 [89] P. Andric and W. Curtin, Atomistic modeling of fracture, Modelling and Simulation in Ma-
1017 terials Science and Engineering **27**, 013001 (2018).
- 1018 [90] J. Song, W. Curtin, T. Bhandakkar, and H. Gao, Dislocation shielding and crack tip decohesion
1019 at the atomic scale, Acta Materialia **58**, 5933 (2010).
- 1020 [91] E. Mak and W. A. Curtin, Intrinsic fracture behavior of mg-y alloys, Modelling and Simulation
1021 in Materials Science and Engineering **28**, 035012 (2020).
- 1022 [92] J.-J. Tang, X.-B. Yang, L. OuYang, M. Zhu, and Y.-J. Zhao, A systematic first-principles
1023 study of surface energies, surface relaxation and friedel oscillation of magnesium surfaces,
1024 Journal of Physics D: Applied Physics **47**, 115305 (2014).